

# Modeling NK-cell lymphoma in mice reveals its cell-of-origin and microenvironmental changes and identifies therapeutic targets

Received: 27 February 2024

Accepted: 10 October 2024

Published online: 22 October 2024

 Check for updates

A list of authors and their affiliations appears at the end of the paper

Extranodal NK/T-cell lymphoma (ENKTCL) is an Epstein-Barr virus (EBV)-related neoplasm preferentially involving the upper aerodigestive tract. Here we show that NK-cell-specific *Trp53* disruption in mice leads to the development of NK-cell lymphomas after long latency, which involve not only the hematopoietic system but also the salivary glands. Before tumor onset, *Trp53* knockout causes extensive gene expression changes, resulting in immature NK-cell expansion, exclusively in the salivary glands. Both human and murine NK-cell lymphomas express tissue-resident markers, suggesting tissue-resident NK cells as their cell-of-origin. Murine NK-cell lymphomas show recurrent *Myc* amplifications and upregulation of MYC target gene signatures. EBV-encoded latent membrane protein 1 expression accelerates NK-cell lymphomagenesis and causes diverse microenvironmental changes, particularly myeloid propagation, through interferon- $\gamma$  signaling. In turn, myeloid cells support tumor cells via CXCL16-CXCR6 signaling and its inhibition is effective against NK-cell tumors in vivo. Remarkably, KLRG1-expressing cells expand in the tumor and are capable of repopulating tumors in secondary recipients. Furthermore, targeting KLRG1 alone or combined with MYC inhibition using an eIF4 inhibitor is effective against NK-cell tumors. Therefore, our observations provide insights into the pathogenesis and highlight potential therapeutic targets, including CXCL16, KLRG1, and MYC, in ENKTCL, which can help improve its diagnostic and therapeutic strategies.

Extranodal NK/T-cell lymphoma (ENKTCL) is an aggressive NK/T-cell neoplasm, which is characterized by angiodestruction, cytotoxic phenotype, and constant association with Epstein-Barr virus (EBV)<sup>1,2</sup>. ENKTCL is prevalent among Asian and South American populations and preferentially involves the upper aerodigestive tract, including the nasal cavity and nasopharynx. However, what mechanisms underlie such site predilection and which NK-cell subpopulation is responsible for ENKTCL remain unclear. The therapeutic approach to ENKTCL presents substantial challenges<sup>2,3</sup>; traditional chemotherapy is ineffective due to P-glycoprotein overexpression. Despite the use of current standard regimens containing L-asparaginase, advanced-stage ENKTCL has a poor prognosis. Therefore, exploring the pathogenic

mechanisms and developing novel therapeutic strategies are required in ENKTCL.

ENKTCL generally expresses latent membrane protein (LMP) 1 and 2 and EBV nuclear antigen 1 (EBNA1)<sup>4-6</sup>. Although their precise oncogenic functions remain unknown, these viral proteins, particularly LMP1, contribute to NK/T-cell transformation. Besides, somatic alterations are essential for the ENKTCL development. Several studies revealed the genetic landscape of ENKTCL and identified recurrent somatic alterations, including those affecting tumor suppressors (such as *TP53*)<sup>7-9</sup>. However, whether and how these viral proteins and genetic alterations contribute to the ENKTCL pathogenesis in vivo remains unclear.

✉ e-mail: [kkataoka-ky@umin.ac.jp](mailto:kkataoka-ky@umin.ac.jp)

ENKTCL is occasionally accompanied by heavy inflammatory cell infiltration<sup>1</sup>. In addition, tumor immune microenvironment subtypes are reported to be associated with disease severity<sup>10,11</sup>. Furthermore, ENKTCL harbors frequent alterations in immune-related molecules, with *CD274* structural variations being the most frequent<sup>8,9</sup>. These observations suggest the importance of the tumor immune microenvironment, but its role and related molecular network remain elusive.

An important limitation of the field is the lack of a genetically engineered mouse model (GEMM) recapitulating genetic events in human ENKTCL. Although cell lines and xenografts have been developed in ENKTCL<sup>12,13</sup>, these models are heterogeneous and unable to reproduce the tumor immune microenvironment.

In this work, to model ENKTCL in mice, we have generated GEMM harboring NK-cell-specific *Trp53* deletion. This model develops NK-cell lymphomas preferentially involving the salivary glands (SG), which is accelerated by *LMP1* expression. Using these models, we reveal the cell-of-origin, microenvironmental changes, and therapeutic targets of ENKTCL.

## Results

### *Trp53* loss induces NK-cell lymphomas frequently involving the salivary glands

To model ENKTCL in mice, we crossed mice carrying two floxed *Trp53* alleles (*Trp53*<sup>lox/lox</sup>) with mice expressing iCre recombinase under the *Ncr1* promoter (*Ncr1-iCre*) to generate NK-cell-specific *Trp53* conditional knockout mice (referred subsequently as *Trp53*<sup>-/-</sup>) (Supplementary Fig. 1a). Most (81.5 %) of *Trp53*<sup>-/-</sup> mice survived more than a year but died earlier than wild-type (WT) mice, with a median survival of 417 days (Fig. 1a). Complete blood count (CBC) showed mild leukocytosis, anemia, and thrombocytopenia in *Trp53*<sup>-/-</sup> mice (Fig. 1b). Macroscopic evaluation demonstrated the enlargement of the SG, in addition to hepatosplenomegaly and occasional abdominal mass, in *Trp53*<sup>-/-</sup> mice (Fig. 1c and Supplementary Fig. 1b), suggesting that these mice developed a lethal hematopoietic neoplasm involving the SG.

Histological examination revealed large-sized atypical lymphoid infiltration in the SG and spleen (SP) (Fig. 1d and Supplementary Fig. 1c). Flow cytometry of the tumors identified a population of Lin (Gr1, Ter119, CD19, and CD3)<sup>-</sup>CD122<sup>+</sup>NK1.1<sup>-</sup> cells, suggesting that these tumors were of NK-cell origin (Fig. 1e). The proportion of these cells was significantly increased in both the SG and SP in *Trp53*<sup>-/-</sup> tumor-bearing mice compared with age-matched WT controls (Fig. 1f and Supplementary Fig. 1d). These cells also expressed NK-cell transcription factors (such as Eomes and T-bet), consistent with a recent report analyzing human ENKTCL<sup>13</sup>. They also showed variable expressions of lineage-committed NK-cell markers (such as CD43, CD146 [MCAM], CD226 [DNAM1], and Ly6C), but had no or almost no expressions of CD62L and CD11b (Fig. 1g and Supplementary Fig. 1e). To confirm their lymphomagenic potential, we transplanted *Trp53*<sup>-/-</sup> tumor cells into lethally irradiated recipients, all of which developed NK-cell tumors and died within 77 days (Fig. 1h). Taken together, NK-cell-specific *Trp53* disruption induces transplantable NK-cell lymphomas after long latency that frequently involve the SG and the hematopoietic system.

### *Trp53* disruption predominantly affects tissue-resident NK cells in the salivary glands

SG NK cells are tissue-resident NK cells that are distinct from conventional NK cells in the peripheral blood (PB), SP, and bone marrow (BM)<sup>14</sup>. To determine the cell-of-origin of *Trp53*<sup>-/-</sup> NK-cell lymphomas, we investigated whether and how *Trp53* deficiency has different effects on NK cells across these tissues in the pre-tumor state. CBC showed no differences between WT and *Trp53*<sup>-/-</sup> mice at eight weeks old (Supplementary Fig. 2a, b). Remarkably, *Trp53*<sup>-/-</sup> mice exhibited increased Lin<sup>-</sup>CD122<sup>+</sup>NK1.1<sup>-</sup> cells and decreased Lin<sup>-</sup>CD122<sup>+</sup>NK1.1<sup>-</sup>CD11b<sup>+</sup> cells in the SG, while there was no difference in the frequency of NK-cell

subpopulations in the SP and BM between WT and *Trp53*<sup>-/-</sup> mice (Fig. 2a and Supplementary Fig. 2c), suggesting that *Trp53* disruption increases immature NK cells exclusively in the SG. Cell-cycle analysis revealed an increase of Ki-67<sup>+</sup> cells only in the SG from *Trp53*<sup>-/-</sup> mice, with no difference in the SP and BM (Fig. 2b and Supplementary Fig. 2d). By contrast, there was no difference in the apoptotic status in all examined tissues (Supplementary Fig. 2e). These results suggest that *Trp53* deficiency exerts differential effects on conventional circulating NK cells in the SP and BM and tissue-resident NK cells in the SG.

To investigate gene expression profiles underlying phenotypic differences in NK cells across tissues, we performed RNA-sequencing (RNA-seq) analysis of Lin<sup>-</sup>CD122<sup>+</sup> NK cells from the SG, SP, and BM of WT and *Trp53*<sup>-/-</sup> mice (Supplementary Fig. 2f). Importantly, there were almost no differentially expressed genes between WT and *Trp53*<sup>-/-</sup> NK cells in the SP and BM, whereas 81 genes were upregulated in *Trp53*<sup>-/-</sup> SG NK cells (Fig. 2c). Gene set enrichment analysis (GSEA) demonstrated overrepresentation of extracellular matrix (ECM)-associated signatures exclusively in the SG (Fig. 2d, Supplementary Fig. 2g, h, and Supplementary Data 1). We also evaluated RNA-seq of human samples, which revealed upregulation of 162 signatures in ENKTCL tumors compared with normal NK cells (Supplementary Data 2, 3). Among them, 15 signatures were related to ECM dynamics (Supplementary Fig. 2i and Supplementary Data 3). These results suggest that *Trp53* disruption induces ECM-associated transcriptomic changes in the SG, which are characteristic of ENKTCL.

The predominant effect of *Trp53* disruption on tissue-resident NK cells in the SG led us to evaluate characteristic phenotypes of tissue-resident NK cells in *Trp53*<sup>-/-</sup> tumors. Similar to SG NK cells, these tumors highly expressed tissue-resident markers, such as CD69 and CD49a<sup>14</sup>, in both the SG and SP (Fig. 2e). We then evaluated the origin of human ENKTCL cells using RNA-seq data, which demonstrated upregulation of a tissue-resident NK-cell signature, including *ITGAI* (encoding CD49a) and *CCR5* expressions, and downregulation of a circulating NK-cell signature, including *SIPRS* and *CX3CRI* expressions, in ENKTCL tumors (Fig. 2f, Supplementary Fig. 2j, and Supplementary Data 4). High expression of CD49a was detected in human ENKTCL by immunohistochemistry (Fig. 2g and Supplementary Fig. 2k). These results suggest that human and murine ENKTCL cells are derived from tissue-resident NK cells.

### NK-cell tumors show genomic and transcriptomic alterations involving *Myc*

To investigate genetic profiles of *Trp53*<sup>-/-</sup> tumors, we performed whole-exome sequencing (WES), which confirmed the clonality (defined as having >3 mutations) in 7 out of 11 tumors (Supplementary Fig. 3a–c). Although these tumors harbored a median number of 23 (range, 11–61) non-synonymous mutations, the mutant allele frequency was generally low, suggestive of low tumor content. These tumors showed a similar pattern of copy number alterations (CNAs), probably reflecting the *Trp53*-induced genomic instability (Supplementary Fig. 3d). Particularly, two *Trp53*<sup>-/-</sup> tumors harbored focal amplifications involving *Myc*, whose activation is frequently observed in human ENKTCL<sup>9,15</sup>. By contrast, no CNAs were detected in the remaining four tumors. The absence of the *Trp53* deletion confirmed no or few neoplastic cells in these tumors (Supplementary Fig. 3b). However, despite the slightly longer latency, all recipients transplanted with clonally unconfirmed tumor cells developed NK-cell neoplasms (Supplementary Fig. 3e). Moreover, WES analysis detected somatic alterations in secondary tumors (Supplementary Fig. 3c), suggesting that these tumors contain a small proportion of neoplastic clonal cells. RNA-seq showed the significant enrichment of proliferation-related and MYC target gene signatures in *Trp53*<sup>-/-</sup> tumors (Supplementary Fig. 3f and Supplementary Data 5), which is consistent with upregulated signatures in human *TP53*-mutated ENKTCL samples (Supplementary

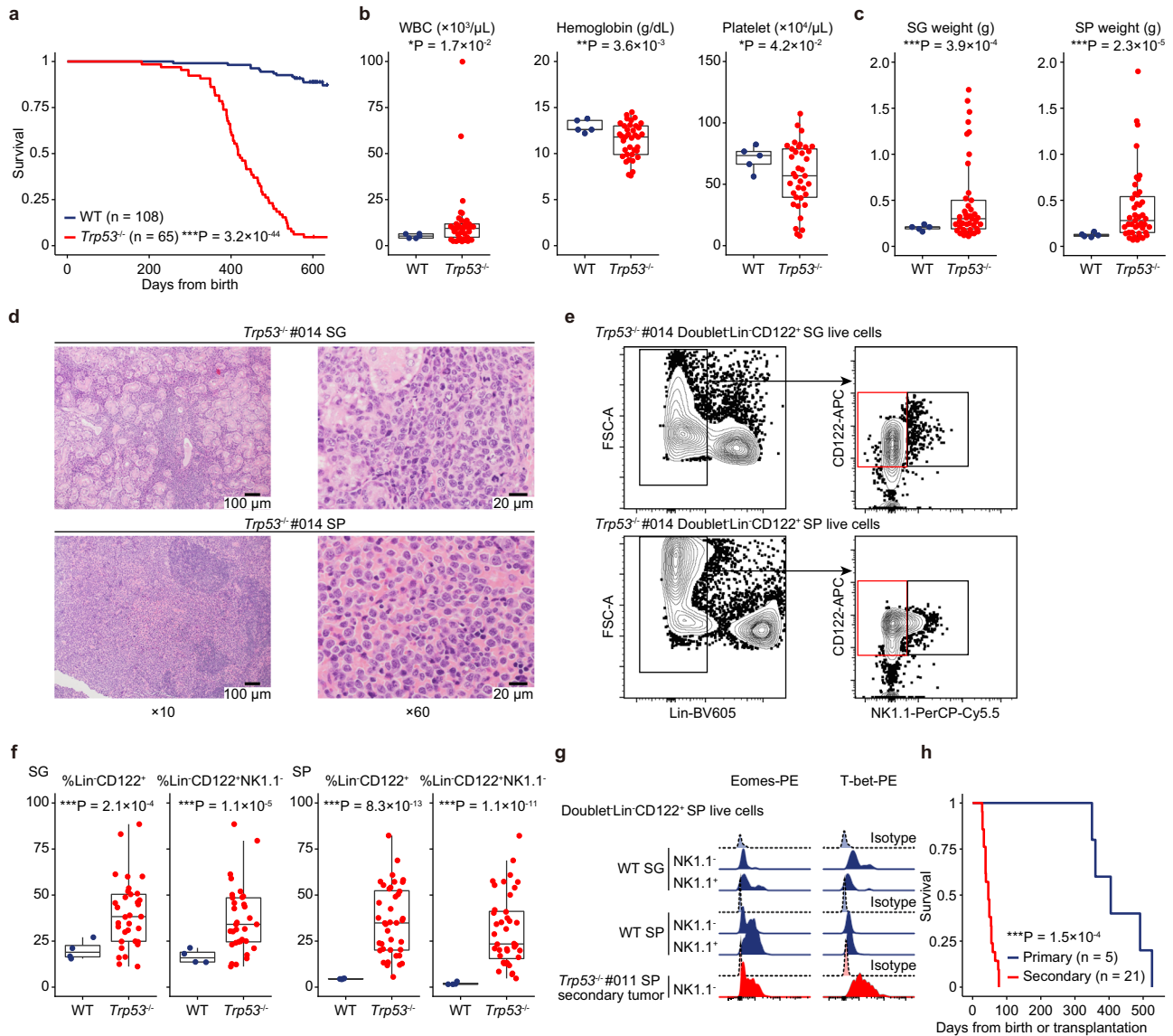


**Fig. 1 | Targeted disruption of *Trp53* causes NK-cell lymphomas after long latency.** **a** Kaplan–Meier survival curves of WT (n = 108) and *Trp53*<sup>-/-</sup> (n = 65) mice. Log-rank test. **b** CBC in PB of WT (n = 5 at 60 weeks old) and *Trp53*<sup>-/-</sup> (n = 37 at tumor onset) mice. **c** SG and SP weights of WT (n = 5 at 60 weeks old) and *Trp53*<sup>-/-</sup> (n = 41 at tumor onset) mice. **d** Representative images of hematoxylin and eosin staining of *Trp53*<sup>-/-</sup> tumors in SG and SP. **e** Representative plots of immature NK cells (Lin<sup>-</sup>CD122<sup>+</sup>NK1.1<sup>+</sup>) in *Trp53*<sup>-/-</sup> tumors in SG and SP. **f** Proportion of Lin<sup>-</sup>CD122<sup>+</sup> and Lin<sup>-</sup>CD122<sup>+</sup>NK1.1<sup>+</sup> cells in SG (n = 4) and SP (n = 4) from WT (at 60 weeks old) and in SG (n = 33) and SP (n = 40) from *Trp53*<sup>-/-</sup> (at tumor onset) mice. **g** Representative

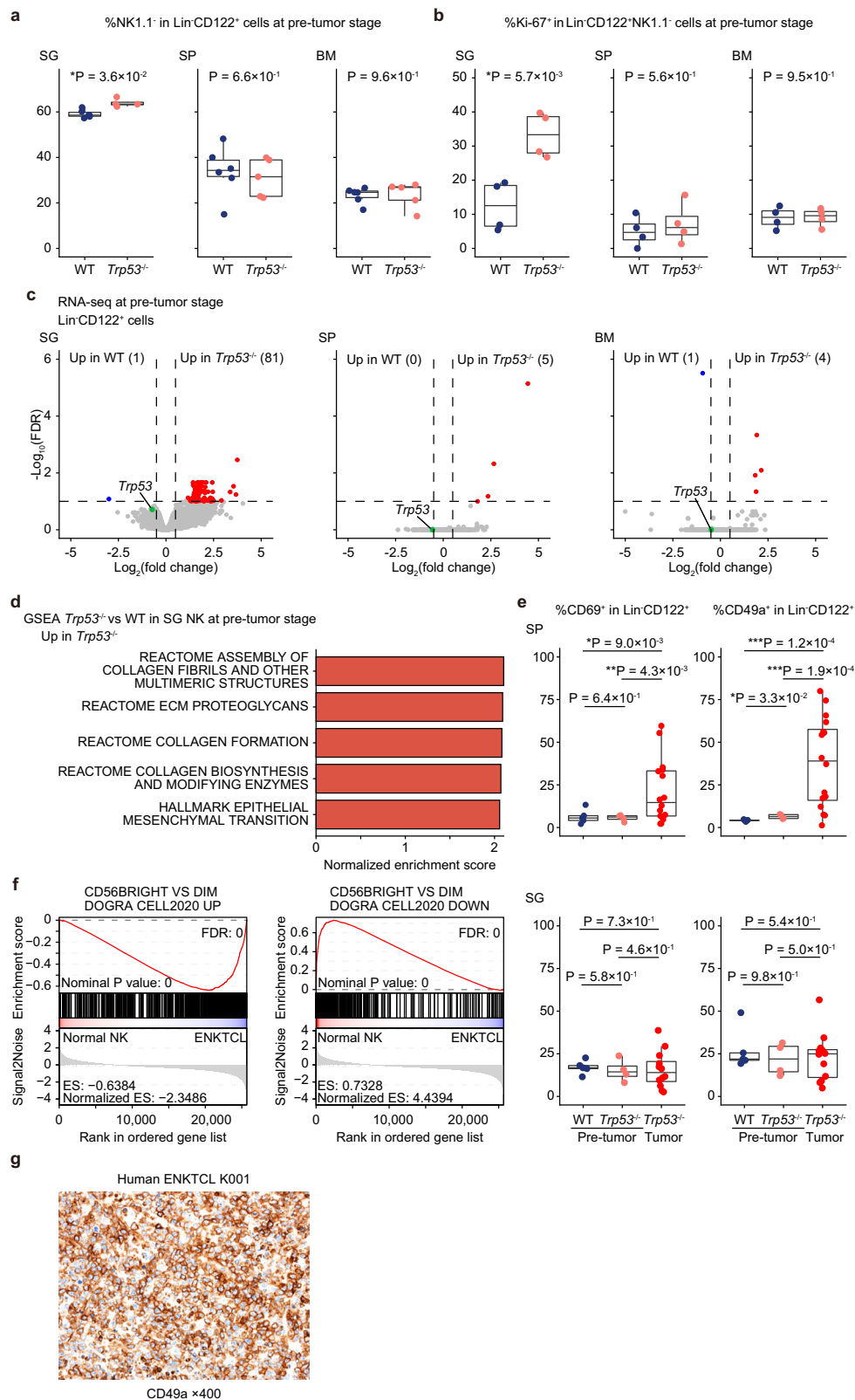
histograms of Eomes and T-bet expression in Lin<sup>-</sup>CD122<sup>+</sup>NK1.1<sup>-</sup> and Lin<sup>-</sup>CD122<sup>+</sup>NK1.1<sup>+</sup> cells in SG and SP from WT mice (at 8 weeks old) and *Trp53*<sup>-/-</sup> secondary tumors in SP. Isotype controls are shown as shaded histograms. **h** Kaplan–Meier survival curves of secondary mice (n = 21) transplanted with 1 × 10<sup>6</sup> *Trp53*<sup>-/-</sup> tumor cells compared with the corresponding primary mice. (n = 5). Log-rank test. **b**, **c**, and **f** Box plots show medians (lines), IQRs (boxes), and ±1.5 × IQR (whiskers). \*P < 0.05, \*\*P < 0.005, \*\*\*P < 0.0005, two-sided Welch's t-test. **a**, **b**, **c**, **f**, and **h** Source data are provided as a Source Data file.

Fig. 3g and Supplementary Data 6). These results suggest that *Myc* is genomically and/or transcriptionally deregulated in *Trp53*-deficient NK-cell tumors.

### LMP1 accelerates the tumor development and alters the immune microenvironment

Although EBV-encoded LMP1 is involved in ENKTCL pathogenesis<sup>4–6</sup>, its in vivo role in NK-cell lymphomagenesis remains unknown. To address this, we crossed *Ncr1-iCre*; *Trp53*<sup>fllox/fllox</sup> (*Trp53*<sup>-/-</sup>) mice to *LMP1*<sup>stop</sup> conditional knock-in (*LMP1*<sup>+</sup>) mice to generate *Ncr1-iCre*; *Trp53*<sup>fllox/fllox</sup>; *LMP1*<sup>stop</sup> (*Trp53*<sup>-/-</sup>*LMP1*<sup>+</sup>). *Trp53*<sup>-/-</sup>*LMP1*<sup>+</sup> mice developed a lethal NK-cell lymphoma with a median survival of 258 days, which was significantly shorter than that of mice with either disease allele alone (*Trp53*<sup>-/-</sup> or *LMP1*<sup>+</sup>) (Fig. 3a). Thus, *Trp53* loss and *LMP1* expression

cooperate to induce NK-cell lymphomagenesis. We observed severer thrombocytopenia in *Trp53*<sup>-/-</sup>*LMP1*<sup>+</sup> mice than *Trp53*<sup>-/-</sup> mice, while there was no difference in WBC and hemoglobin counts and the extent of organ enlargement (Fig. 3b and Supplementary Fig. 4a). Consistent with *Trp53*<sup>-/-</sup> tumors, flow cytometric analysis showed a population of Lin<sup>-</sup>CD122<sup>+</sup>NK1.1<sup>+</sup> cells in *Trp53*<sup>-/-</sup>*LMP1*<sup>+</sup> tumors (Supplementary Fig. 4b). Pathologically, *Trp53*<sup>-/-</sup>*LMP1*<sup>+</sup> tumors showed more extensive myeloid infiltration and coagulative necrosis associated with vascular destruction, resembling the pathology of human ENKTCL (Fig. 3c and Supplementary Fig. 4c). WES analysis showed a comparable number of somatic mutations between *Trp53*<sup>-/-</sup> and *Trp53*<sup>-/-</sup>*LMP1*<sup>+</sup> tumors (Fig. 3d and Supplementary Fig. 4d). By contrast, *Trp53*<sup>-/-</sup>*LMP1*<sup>+</sup> tumors had a significantly smaller number of CNAs than *Trp53*<sup>-/-</sup> tumors, although a similar CNA pattern, including *Myc* amplification, was observed



between them (Fig. 3d and Supplementary Fig. 4e–g). These results suggest that *LMP1* expression can substitute for secondary CNAs in NK-cell lymphomagenesis. We next characterized mutational processes in murine NK-cell tumors and revealed that clock-like (84.7%) and reactive oxygen species (15.3%) signatures were dominant, which is highly concordant with those found in human ENKTCL (Supplementary Fig. 4h).

### Diverse changes in the multicellular ecosystem of murine NK-cell tumors

As neoplastic tumor cells accounted for only a limited fraction of cells, we elucidated the complexity of the tumor immune microenvironment of murine NK-cell tumors. We constructed single-cell (sc) transcriptomic maps of 18,542 malignant and 66,008 nonmalignant CD45<sup>+</sup> cells from 9 *Trp53*<sup>-/-</sup> and 4 *Trp53*<sup>-/-</sup>*LMP1*<sup>+</sup> tumors and SG and SP from 2

**Fig. 2 | Differential effects of *Trp53* disruption on NK cells across tissues at the pre-tumor stage.** **a** Proportion of NK1.1<sup>+</sup> cells in Lin<sup>+</sup>CD122<sup>+</sup> cells in SG, SP, and BM from WT (n = 6) and *Trp53*<sup>-/-</sup> (n = 5) mice (at 8 weeks old). **b** Proportion of Ki-67<sup>+</sup> cells in Lin<sup>+</sup>CD122<sup>+</sup>NK1.1<sup>+</sup> cells in SG, SP, and BM from WT (n = 4) and *Trp53*<sup>-/-</sup> (n = 4) mice (at 8 weeks old). **c** Volcano plots showing differentially expressed genes between WT and *Trp53*<sup>-/-</sup> Lin<sup>+</sup>CD122<sup>+</sup> NK cells in SG, SP, and BM (at 8 weeks old). Genes with FDR < 0.1 and |log<sub>2</sub>(fold change)| ≥ 0.5 are considered significant and colored red (upregulated) or blue (downregulated). **d** The top five upregulated signatures in GSEA analysis of expression data comparing WT (n = 5) and *Trp53*<sup>-/-</sup> (n = 3) Lin<sup>+</sup>CD122<sup>+</sup> NK cells in SG (at 8 weeks old). Signatures with FDR < 0.25 are

considered significant. **e** Proportion of CD69<sup>+</sup> and CD49a<sup>+</sup> cells in Lin<sup>+</sup>CD122<sup>+</sup> NK cells in SG (n = 5 at 8 weeks old) and SP (n = 5 at 8 weeks old) from WT and in SG (n = 6 at 8 weeks old and n = 12 at tumor onset) and SP (n = 6 at 8 weeks old and n = 16 at tumor onset) from *Trp53*<sup>-/-</sup> mice. **f** Significant enrichment of tissue-resident (left) and circulating (right) NK-cell signatures in GSEA analysis of expression data comparing human normal NK cells (n = 4) and ENKTCL tumors (n = 41). **g** Representative image of CD49a immunostaining in a human ENKTCL sample. **a**, **b**, and **e**, Box plots show medians (lines), IQRs (boxes), and ±1.5× IQR (whiskers). \*P < 0.05, \*\*P < 0.005, \*\*\*P < 0.0005, two-sided Welch's t-test. No adjustments were made for multiple comparisons. Source data are provided as a Source Data file.

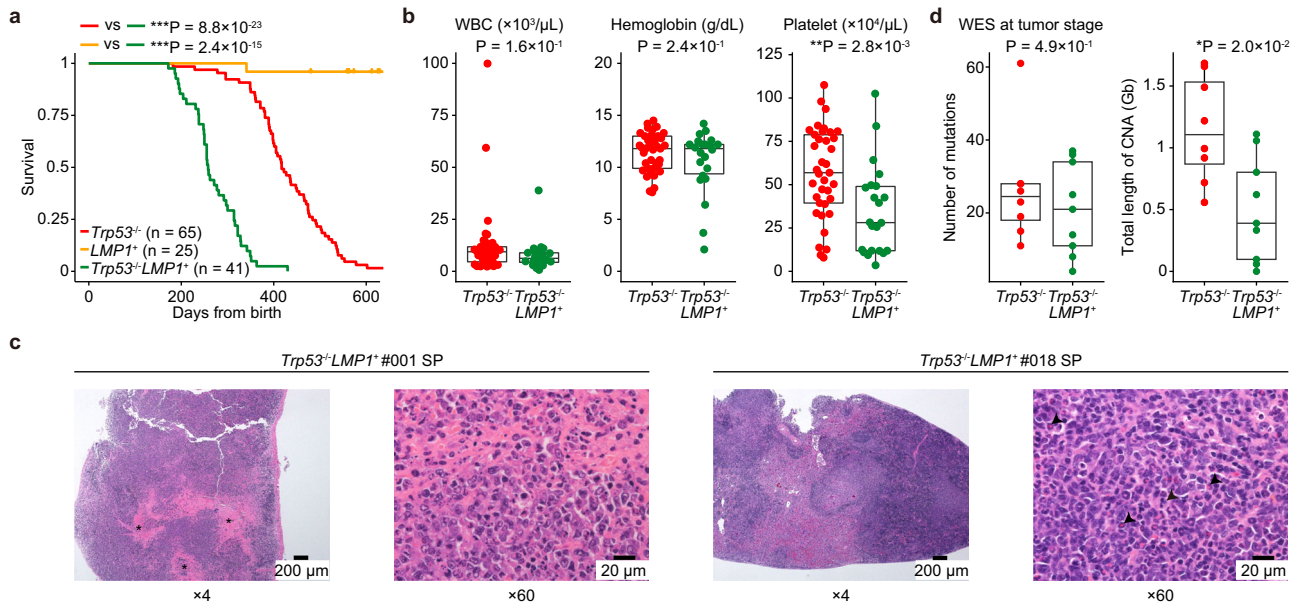


**Fig. 3 | Combined effects of *Trp53* loss and *LMP1* expression on normal and malignant NK cells.** **a** Kaplan–Meier survival curves of *Trp53*<sup>-/-</sup> (n = 65), *LMP1*<sup>+</sup> (n = 25), and *Trp53*<sup>-/-</sup>*LMP1*<sup>+</sup> (n = 41) mice. Log-rank test. No adjustments were made for multiple comparisons. *Trp53*<sup>-/-</sup> data are the same as in Fig. 1a. **b** CBC in PB of *Trp53*<sup>-/-</sup> (n = 37) and *Trp53*<sup>-/-</sup>*LMP1*<sup>+</sup> (n = 22) mice (at tumor onset). *Trp53*<sup>-/-</sup> data are the same as in Fig. 1b. **c** Representative image of hematoxylin and eosin staining of

*Trp53*<sup>-/-</sup>*LMP1*<sup>+</sup> tumors in SP. Asterisks and arrowheads show coagulative necrosis and myeloid infiltration, respectively. **d** Number of somatic mutations and total length of CNAs per sample in *Trp53*<sup>-/-</sup> (n = 7) and *Trp53*<sup>-/-</sup>*LMP1*<sup>+</sup> (n = 9) tumors detected by WES. **b**, **d** Box plots show medians (lines), IQRs (boxes), and ±1.5× IQR (whiskers). \*P < 0.05, \*\*P < 0.005, \*\*\*P < 0.0005, two-sided Welch's t-test. **a**, **b**, and **d** Source data are provided as a Source Data file.

WT and 2 *Trp53*<sup>-/-</sup> mice at pre-tumor stage, identifying 20 clusters, consisting of 7 malignant and 13 nonmalignant ones (Fig. 4a, b, Supplementary Fig. 5a–f, and Supplementary Data 7, 8). Nonmalignant clusters accounted for the majority of cells and consisted of 2 T-cell, 4 B-cell, 1 NK-cell, and 5 myeloid cell clusters based on canonical lineage markers. Compared with pre-tumor samples, *Trp53*<sup>-/-</sup> tumors exhibited a decreased proportion of CD4<sup>+</sup> and CD8<sup>+</sup> T cells, NK cells, and myeloid cells, while B cells were slightly increased in the extranodal tissues (including the SG and other sites) and SP (Fig. 4c). Importantly, myeloid cells were markedly increased in both SG and SP from *Trp53*<sup>-/-</sup>*LMP1*<sup>+</sup> tumors, whereas the proportion of other nonmalignant clusters was almost comparable between *Trp53*<sup>-/-</sup> and *Trp53*<sup>-/-</sup>*LMP1*<sup>+</sup> tumors (Supplementary Data 9). These findings were confirmed by flow cytometric analysis (Fig. 4d). In addition, deconvolution of RNA-seq data of human ENKTCL revealed that myeloid cell infiltration was observed in all tumors, with significantly higher proportions compared with normal tonsils (Supplementary Fig. 5g, h and Supplementary Data 10). These observations suggest that *LMP1* predominantly induces myeloid propagation in the tumor microenvironment.

To further characterize immune cell clusters, we performed subclustering, which identified 3 CD4<sup>+</sup> T-cell (naive, effector/memory [EM], and Treg), 5 CD8<sup>+</sup> T-cell (naive, central/memory [CM], EM, resident/memory [RM], and exhausted [EX]), and 3 B-cell (immature, mature, and plasmablasts) subclusters (Supplementary Fig. 5i, j and

Supplementary Data 8). Both *Trp53*<sup>-/-</sup> and *Trp53*<sup>-/-</sup>*LMP1*<sup>+</sup> tumors showed decreased naive T cells, whereas CD8<sup>+</sup> T EX cells were increased in the extranodal tissues from *Trp53*<sup>-/-</sup>*LMP1*<sup>+</sup> tumors (Fig. 4c and Supplementary Data 9), suggesting enhanced T-cell exhaustion in *Trp53*<sup>-/-</sup>*LMP1*<sup>+</sup> tumors.

### ***LMP1* induces massive expansion of tumor-promoting myeloid cells**

As the most prominent change in the tumor microenvironment was myeloid expansion by *LMP1* expression, we focused on myeloid clusters in NK-cell tumors. The myeloid subclusters included monocyte (Mono), macrophage (Macro), type 1 and 2 conventional dendritic cell (cDC1 and cDC2), plasmacytoid DC (pDC), mature DC enriched in immunoregulatory molecules (mregDC), and myeloid-derived suppressor cell (MDSC) (Fig. 5a, Supplementary Fig. 6a, and Supplementary Data 8). A higher proportion of Mono and cDC1 were observed in *Trp53*<sup>-/-</sup>*LMP1*<sup>+</sup> tumors from both the extranodal tissues and SP, whereas MDSC was strongly enriched in the SP (Fig. 5b and Supplementary Data 9). By contrast, Macro, pDC, and mregDC were decreased in the SP from *Trp53*<sup>-/-</sup>*LMP1*<sup>+</sup> tumors. The increase of cDC1 was confirmed by flow cytometric analysis (Supplementary Fig. 6b). GSEA analysis showed upregulation of metabolic pathways in various myeloid subclusters from *Trp53*<sup>-/-</sup> tumors (Fig. 5c and Supplementary Data 11). On the other hand, interferon (IFN)-α/γ response and TNFα/

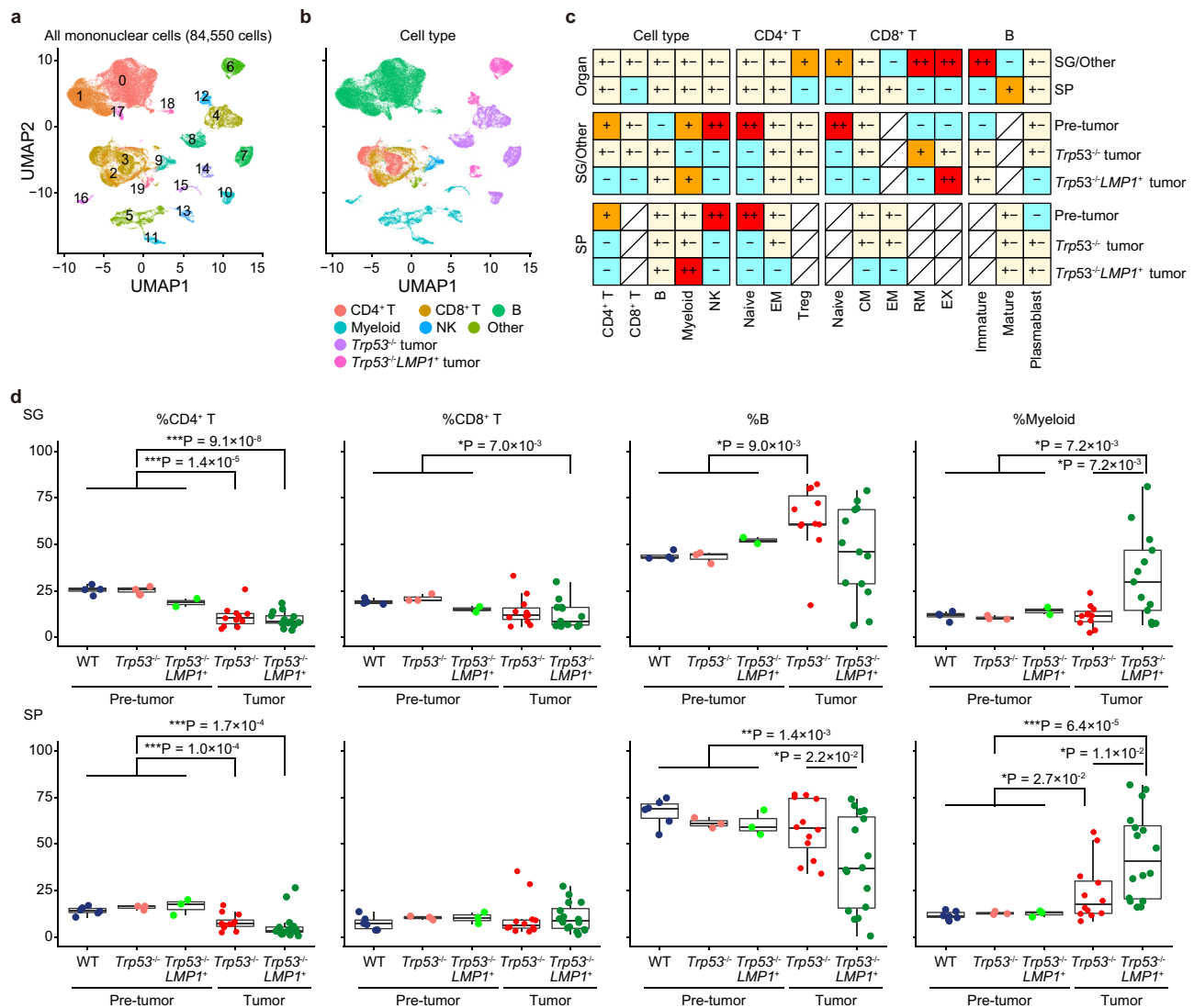


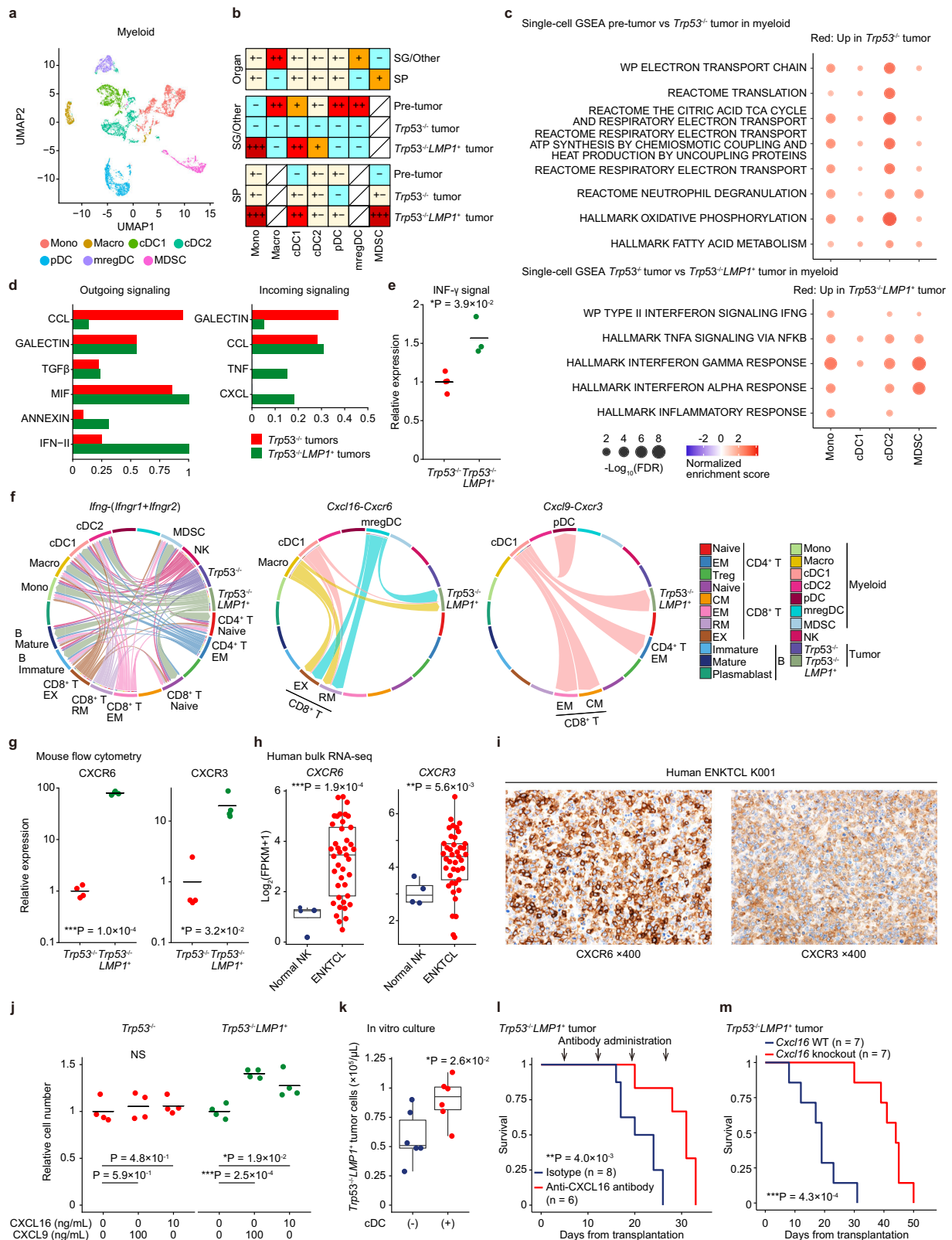
**Fig. 4 | Single-cell analysis reveals dynamic changes in the tumor microenvironment in NK-cell tumors.** **a** UMAP plot of 84,550 CD45<sup>+</sup> mononuclear cells from SG and SP of WT (n=1) and *Trp53*<sup>-/-</sup> (n=1) mice at the pre-tumor stage (at 8 weeks old), *Trp53*<sup>-/-</sup> tumors in SG (n=3) and SP (n=6), and *Trp53*<sup>-/-</sup>*LMP1*<sup>+</sup> tumors in other sites (n=2) and SP (n=2). Seven malignant and 13 nonmalignant clusters are shown in different colors. **b** UMAP plot (same as **a**) colored by cell type. **c** The distribution of broad and specific cell types in each group in SG and SP revealed by  $R_{o/e}$  analysis (ratio of observed cell number to expected cell number). ++,  $2 \leq R_{o/e} < 3$ ; +,  $1.5 \leq R_{o/e} < 2$ ; +/-,  $0.67 \leq R_{o/e} < 1.5$ ; -,  $0 \leq R_{o/e} < 0.67$ . **d** Proportion of

CD4<sup>+</sup> T, CD8<sup>+</sup> T, B, and myeloid cells from SG (n=4) and SP (n=6) of WT, SG (n=3) and SP (n=3) of *Trp53*<sup>-/-</sup>, and SG (n=2) and SP (n=3) of *Trp53*<sup>-/-</sup>*LMP1*<sup>+</sup> mice at the pre-tumor stage (at 8 weeks old), *Trp53*<sup>-/-</sup> tumors in SG (n=11) and SP (n=12), and *Trp53*<sup>-/-</sup>*LMP1*<sup>+</sup> tumors in SG (n=13) and SP (n=16). Proportion in nonmalignant cells is shown for tumor-bearing mice. Box plots show medians (lines), IQRs (boxes), and  $\pm 1.5 \times$  IQR (whiskers). \* $P < 0.05$ , \*\* $P < 0.005$ , \*\*\* $P < 0.0005$ , two-sided Welch's t-test. Only significant P values ( $< 0.05$ ) are shown. No adjustments were made for multiple comparisons. Source data are provided as a Source Data file.

NF- $\kappa$ B signaling were upregulated in *Trp53*<sup>-/-</sup>*LMP1*<sup>+</sup> tumors (Fig. 5c and Supplementary Data 12). IFN- $\gamma$  response activation was also observed in several T- and B-cell subclusters (Supplementary Fig. 6c and Supplementary Data 12), suggesting that enhanced IFN- $\gamma$  signaling is pervasive across immune cells of *Trp53*<sup>-/-</sup>*LMP1*<sup>+</sup> tumors. Then, we inferred cell-cell interactions using CellChat, which showed that IFN-II signaling (including only IFN- $\gamma$ ) was the most upregulated outgoing signaling in *Trp53*<sup>-/-</sup>*LMP1*<sup>+</sup> tumor cells compared with *Trp53*<sup>-/-</sup> tumor cells (Fig. 5d, Supplementary Fig. 6d, and Supplementary Data 13). Comparison of the information flow between *Trp53*<sup>-/-</sup> and *Trp53*<sup>-/-</sup>*LMP1*<sup>+</sup> tumors confirmed the highest upregulation of IFN-II signaling (Supplementary Fig. 6e). Intracellular flow cytometry confirmed elevated IFN- $\gamma$  protein expression in *Trp53*<sup>-/-</sup>*LMP1*<sup>+</sup> tumor cells (Fig. 5e and Supplementary Fig. 6f). IFN-II signal was mainly transmitted to myeloid cells, including Mono and cDC1 (Fig. 5f). Given LMP1 induces IFN- $\gamma$  production and secretion<sup>16</sup>, these results suggest that LMP1-mediated IFN- $\gamma$  signaling is

a dominant contributor of microenvironmental changes, particularly myeloid expansion, in *Trp53*<sup>-/-</sup>*LMP1*<sup>+</sup> tumors.

Next, we investigated how altered immune cells affect *Trp53*<sup>-/-</sup>*LMP1*<sup>+</sup> tumor cells in the tumor microenvironment. Among the incoming signaling to tumor cells, CXC chemokine ligand (CXCL) signaling was significantly upregulated in *Trp53*<sup>-/-</sup>*LMP1*<sup>+</sup> tumor cells compared with *Trp53*<sup>-/-</sup> tumor cells (Fig. 5d, Supplementary Fig. 6d, and Supplementary Data 13). This signaling included *Cxcl16-Cxcr6* and *Cxcl9-Cxcr3* signaling, which was mainly derived from myeloid cells, especially from cDC1 (Fig. 5f). Flow cytometric analysis confirmed higher expressions of CXCR6 and CXCR3 in *Trp53*<sup>-/-</sup>*LMP1*<sup>+</sup> tumor cells (Fig. 5g and Supplementary Fig. 6g). RNA-seq of human samples showed increased expressions of these chemokine ligands and receptors and their correlation with *LMP1* expression in ENKTC1 (Fig. 5h and Supplementary Fig. 6h, i). We also validated the presence of CD11c<sup>+</sup> DC in the tumor microenvironment and CXCR6 and CXCR3



protein expressions in tumor cells by immunohistochemical analysis of human ENKTCL (Fig. 5i and Supplementary Fig. 6j). We next investigated whether chemokine signaling from myeloid cells can support the development of NK-cell tumors. First, we examined the effect of CXCL16 or CXCL9 in vitro and found that these chemokines supported the expansion of *Trp53*<sup>-/-</sup>*LMP1*<sup>+</sup> tumor cells (Fig. 5j). Then, we performed co-culture with cDC in vitro, which was found to promote

proliferation of *Trp53*<sup>-/-</sup>*LMP1*<sup>+</sup> tumor cells (Fig. 5k). Then, we administered anti-CXCL16 antibody to mice transplanted with *Trp53*<sup>-/-</sup>*LMP1*<sup>+</sup> tumor cells. This treatment significantly prolonged the survival of the tumor-bearing mice (Fig. 5l). Similar findings were obtained when *Trp53*<sup>-/-</sup>*LMP1*<sup>+</sup> tumor cells were transplanted into *Cxcl16* knockout mice (Fig. 5m). These results point to the crucial role of CXCL16-CXCR6 signaling and related myeloid lineage in NK-cell lymphomagenesis.

**Fig. 5 | *LMP1* causes prominent myeloid propagation supporting malignant NK-cell proliferation.** **a** UMAP plot of subclustering of myeloid cells. **b** The distribution of myeloid subclusters in each group in the extranodal tissues and SP revealed by  $R_{o/e}$  analysis. +++ indicates  $R_{o/e} \geq 3$ ; ++,  $2 \leq R_{o/e} < 3$ ; +,  $1.5 \leq R_{o/e} < 2$ ; +/-,  $0.67 \leq R_{o/e} < 1.5$ ; -,  $0 \leq R_{o/e} < 0.67$ . **c** GSEA analysis of scRNA-seq data comparing each myeloid cell subcluster from pre-tumor samples (SG and SP from WT and *Trp53*<sup>-/-</sup> mice) and *Trp53*<sup>-/-</sup> tumor samples (top) and from *Trp53*<sup>-/-</sup> and *Trp53*<sup>-/-</sup>*LMP1*<sup>+</sup> tumor samples (bottom). Signatures significant (FDR < 0.1) across at least two subclusters are shown. **d** Comparison of outgoing and incoming signals between *Trp53*<sup>-/-</sup> and *Trp53*<sup>-/-</sup>*LMP1*<sup>+</sup> tumors in CellChat analysis. **e** Relative IFN- $\gamma$  expressions in Lin<sup>+</sup>CD122<sup>+</sup> cells from *Trp53*<sup>-/-</sup> (n = 4) and *Trp53*<sup>-/-</sup>*LMP1*<sup>+</sup> (n = 3) tumors by intracellular flow cytometry. **f** Chord diagram of *Ifng*-(*Ifngr1*+*Ifngr2*) (left), *Cxcl16*-*Cxcr6* (middle), and *Cxcl9*-*Cxcr3* (right) signaling network across subclusters in *Trp53*<sup>-/-</sup> and *Trp53*<sup>-/-</sup>*LMP1*<sup>+</sup> tumors. **g** Relative CXCR6 (left) and CXCR3 (right) expressions in Lin<sup>+</sup>CD122<sup>+</sup> cells from *Trp53*<sup>-/-</sup> (n = 4) and *Trp53*<sup>-/-</sup>*LMP1*<sup>+</sup> (n = 4) tumors by flow

cytometry. **h** *CXCR6* (left) and *CXCR3* (right) gene expressions in human normal NK cells (n = 4) and ENKTCL tumors (n = 4) by RNA-seq. **i** Representative images of CXCR6 (left) and CXCR3 (right) immunostaining in a human ENKTCL sample. **j** Relative cell number of *Trp53*<sup>-/-</sup> and *Trp53*<sup>-/-</sup>*LMP1*<sup>+</sup> tumor cells 48 h after CXCL16 or CXCL9 treatment at indicated concentrations (n = 4). **k** The number of *Trp53*<sup>-/-</sup>*LMP1*<sup>+</sup> tumor cells after one week of co-culture with and without cDC (n = 6). **l** Kaplan–Meier survival curves of mice transplanted with  $5 \times 10^5$  *Trp53*<sup>-/-</sup>*LMP1*<sup>+</sup> tumor cells and administered with anti-CXCL16 antibody (n = 6) or isotype control (n = 8). Log-rank test. **m** Kaplan–Meier survival curves of WT or *Cxcl16* knockout mice transplanted with  $5 \times 10^5$  *Trp53*<sup>-/-</sup>*LMP1*<sup>+</sup> tumor cells and administered with control vehicle or anti-KLRG1 antibody (n = 7 per group). Log-rank test. **g, j** lines show means. **h, k** Box plots show medians (lines), IQRs (boxes), and  $\pm 1.5 \times$  IQR (whiskers). **e, g, h, j, k** NS: not significant, \*P < 0.05, \*\*P < 0.005, \*\*\*P < 0.0005, two-sided Welch's t-test. No adjustments were made for multiple comparisons. **e, g, h, and j–m** Source data are provided as a Source Data file.

Given that CXCR6 and CXCR3 are tissue-resident NK-cell markers and involved in their retention in specific organs, *Trp53*<sup>-/-</sup>*LMP1*<sup>+</sup> tumor cells leverage a tissue-resident NK-cell phenotype for their maintenance and progression.

### Identification of KLRG1 and MYC as a potential therapeutic target in ENKTCL

These findings led us to hypothesize that dynamic changes in the tumor microenvironment hampered the exploration of tumor cells themselves in bulk sample analysis. Thus, we compared normal and malignant NK cells in scRNA-seq data and found a significant enrichment of proliferation-related, MYC target gene, and metabolic signatures in malignant NK cells in GSEA analysis (Supplementary Fig. 7a and Supplementary Data 14). Among NK-cell markers, tumor cells showed a marked increase in *Klrg1* expression (Fig. 6a). Flow cytometric analysis confirmed an increased proportion of Lin<sup>+</sup>KLRG1<sup>+</sup> and Lin<sup>+</sup>CD122<sup>+</sup>KLRG1<sup>+</sup> cells in *Trp53*<sup>-/-</sup> and *Trp53*<sup>-/-</sup>*LMP1*<sup>+</sup> tumors, although the proportions were slightly lower in *Trp53*<sup>-/-</sup>*LMP1*<sup>+</sup> tumors than in *Trp53*<sup>-/-</sup> tumors, probably due to more extensive inflammatory responses in *Trp53*<sup>-/-</sup>*LMP1*<sup>+</sup> tumors (Fig. 6b and Supplementary Fig. 7b). In addition, the Lin<sup>+</sup>CD122<sup>+</sup>KLRG1<sup>+</sup> fraction correlated with mutant allele frequency in WES (Supplementary Fig. 7c). These results suggest that KLRG1 expression can efficiently capture NK-cell tumor cells. Also, we transplanted Lin<sup>+</sup>KLRG1<sup>+</sup> and Lin<sup>+</sup>KLRG1<sup>+</sup> cells from *Trp53*<sup>-/-</sup> tumors into secondary recipients and found that only Lin<sup>+</sup>KLRG1<sup>+</sup> cells developed into NK-cell tumors (Fig. 6c), suggesting that KLRG1 expression can mark tumor cells. We confirmed that *KLRG1* expression was upregulated in a substantial proportion of ENKTCL samples in human RNA-seq data (Fig. 6d), which was further supported by immunohistochemical analysis showing positive expression of KLRG1 in tumor cells in human ENKTCL, albeit with heterogeneity in KLRG1 positivity across samples. (Fig. 6e and Supplementary Fig. 7d). Then, we examined whether targeting tumor cells with anti-KLRG1 antibody is effective against murine NK-cell tumors and found that anti-KLRG1 antibody treatment reduced the SP size to almost normal in mice transplanted with *Trp53*<sup>-/-</sup> tumors (Supplementary Fig. 7e). In addition, anti-KLRG1 antibody strikingly prolonged the survival of tumor-bearing mice, despite short-term treatment (Fig. 6f). Furthermore, anti-KLRG1 antibody was also effective against *Trp53*<sup>-/-</sup>*LMP1*<sup>+</sup> tumors (Fig. 6g).

As the effectiveness of anti-KLRG1 antibody was modest against *Trp53*<sup>-/-</sup>*LMP1*<sup>+</sup> tumors, we further explored another therapeutic target and identified further upregulation of MYC target gene signature in *Trp53*<sup>-/-</sup>*LMP1*<sup>+</sup> tumors compared with *Trp53*<sup>-/-</sup> tumors in scRNA-seq data (Fig. 6h, Supplementary Fig. 7f and Supplementary Data 15), although the MYC target gene signature was enriched even in *Trp53*<sup>-/-</sup> tumors. Therefore, we administered silvestrol, an eIF4A inhibitor known to inhibit Myc translation<sup>17</sup>, in mice transplanted with *Trp53*<sup>-/-</sup>*LMP1*<sup>+</sup> tumors. This treatment slightly prolonged the survival of

tumor-bearing mice (Fig. 6i). Conspicuously, a combination of anti-KLRG1 antibody and silvestrol further extended the survival (Fig. 6i). These observations suggest that targeting KLRG1 alone and combined with MYC is a promising therapeutic approach against ENKTCL.

### Discussion

Through modeling ENKTCL in mice, we demonstrate that *Trp53* deficiency induces NK-cell neoplasms primarily involving the SG and that *LMP1* expression accelerated their development. Differential effects of *Trp53* loss on tissue-resident NK cells at the pre-tumor stage and high expression of tissue-resident markers in mouse and human NK-cell tumors suggest that tissue-resident NK cells are a putative cell-of-origin of ENKTCL. Among NK-cell transcription factors, T-bet is expressed from NK-cell progenitors and indispensable for the transition from NK-cell progenitors to immature NK cells, while Eomes, together with maturation markers (such as NK1.1 and CD11b), is expressed in mature NK cells and essential for the development of mature NK cells<sup>18</sup>. Therefore, it is difficult to determine which NK-cell maturation stage mouse NK-cell tumors resemble, but *Trp53*-mediated immature NK-cell expansion at the pre-tumor stage implies that these cells are responsible for ENKTCL development. Our findings align with and complement a recent study showing that ENKTCL cells exhibit a similar surface immunophenotype and DNA methylation signature to NK-cell developmental intermediates present in the tonsils and/or peripheral blood, thereby suggesting that ENKTCL cells are arrested at earlier stages of NK-cell maturation<sup>13</sup>. Unlike conventional circulating NK cells, tissue-resident NK cells display a preferential distribution in various non-lymphoid tissues<sup>14</sup>. Probably reflecting interspecies differences, the upper aerodigestive tract is preferentially affected in human ENKTCL, whereas *Trp53*-deficient murine NK-cell tumors predominantly arise from the SG. Tissue-resident NK cells across different tissues have common features, including an immature phenotype and expression of tissue-resident markers and chemokine receptors<sup>14</sup>. Still, these cells show substantial differences with respect to phenotype, function, and transcription factor requirement. Notably, SG NK cells are more susceptible to *Trp53* deficiency-mediated transformation, providing insights into NK-cell heterogeneity and its oncogenesis.

Although *LMP1* is essential for EBV-mediated B-cell transformation in vitro, its expression induces strong cytotoxic T-cell responses in vivo<sup>19,20</sup>. Thus, disruption of immune surveillance is required for B-cell lymphoma development, suggesting a tumor-suppressive role of surrounding T cells. By contrast, our single-cell analyses have uncovered that *LMP1* expression drives myeloid expansion, which can support NK-cell neoplastic proliferation, pointing to a cell-extrinsic, tumor-promoting effect of *LMP1*. Accumulating evidence suggests that myeloid cells are involved in tumor development and progression<sup>21</sup>. In human ENKTCL, tumor-associated macrophages are commonly abundant and their frequency correlates with worse prognosis<sup>10,11,22</sup>. More importantly, mutual crosstalk between NK cells



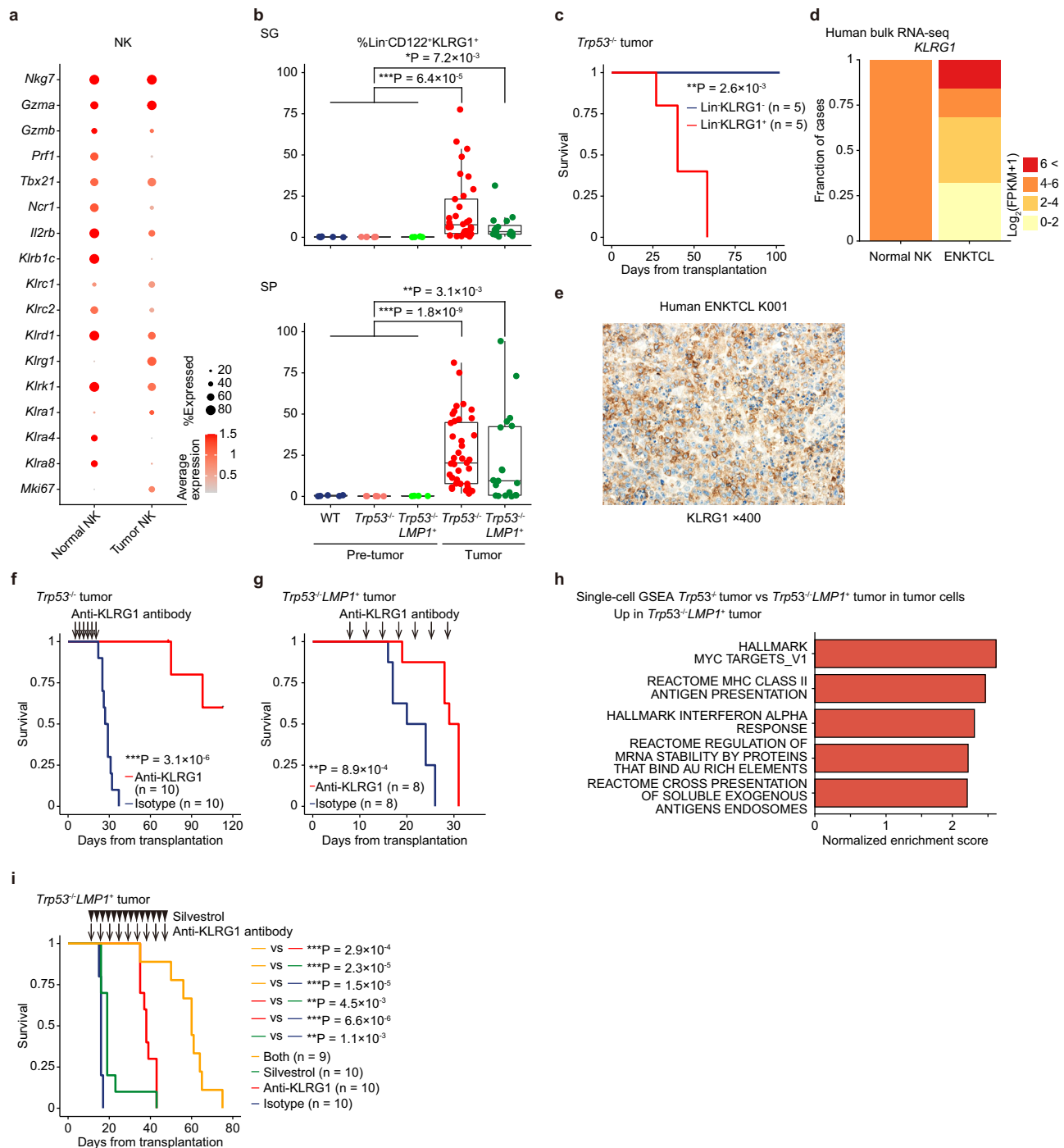


**Fig. 6 | KLRG1 and MYC as potential therapeutic targets in NK-cell neoplasms.**

**a** Bubble plot comparing NK-cell gene expressions between normal and malignant (*Trp53*<sup>-/-</sup> and *Trp53*<sup>-/-</sup>*LMP1*<sup>+</sup>) NK cells in scRNA-seq data. **b** Proportion of Lin<sup>+</sup>CD122<sup>+</sup>KLRG1<sup>+</sup> cells in SG and SP from WT (n = 5 at 8 weeks old and n = 40 at tumor onset), and *Trp53*<sup>-/-</sup>*LMP1*<sup>+</sup> (n = 4 at 8 weeks old and n = 19 at tumor onset) mice. Box plots show medians (lines), IQRs (boxes), and ±1.5 × IQR (whiskers). \*P < 0.05, \*\*P < 0.005, \*\*\*P < 0.0005, two-sided Welch's t-test. Only significant P values (<0.05) are shown. No adjustments were made for multiple comparisons. **c** Kaplan–Meier survival curves of mice transplanted with 2 × 10<sup>4</sup> Lin<sup>+</sup>KLRG1<sup>-</sup> (n = 5) and Lin<sup>+</sup>KLRG1<sup>+</sup> (n = 5) cells from *Trp53*<sup>-/-</sup> NK-cell tumors. Log-rank test. **d** Proportion of human normal NK (n = 4) and ENKTCL samples (n = 41) classified by KLRG1 expression in RNA-seq. **e** Representative image of KLRG1

immunostaining in a human ENKTCL sample. **f, g** Kaplan–Meier survival curves of mice transplanted with 5 × 10<sup>5</sup> *Trp53*<sup>-/-</sup> (**f**) or *Trp53*<sup>-/-</sup>*LMP1*<sup>+</sup> tumor cells (**g**) and administered with anti-KLRG1 antibody or isotype control (n = 10 and n = 8 for *Trp53*<sup>-/-</sup> and *Trp53*<sup>-/-</sup>*LMP1*<sup>+</sup>, respectively). Log-rank test. **h**, GSEA analysis of scRNA-seq data comparing *Trp53*<sup>-/-</sup> and *Trp53*<sup>-/-</sup>*LMP1*<sup>+</sup> malignant NK cells. Top five up-regulated signatures in *Trp53*<sup>-/-</sup>*LMP1*<sup>+</sup> malignant NK cells are shown. Signatures with FDR < 0.25 are considered significant. **i** Kaplan–Meier survival curves of mice transplanted with 5 × 10<sup>5</sup> *Trp53*<sup>-/-</sup>*LMP1*<sup>+</sup> tumor cells and administered with control vehicle, silvestrol, anti-KLRG1 antibody, or both (n = 10 for control, silvestrol, and anti-KLRG1 antibody; n = 9 for both). Log-rank test. No adjustments were made for multiple comparisons. **b, c, f, g,** and **i** Source data are provided as a Source Data file.

and cDC has been well-documented in various immune responses<sup>23,24</sup>. In NK-cell lymphomas, malignant NK cells may hijack this interaction, which can be further augmented by LMP1-induced IFN- $\gamma$  secretion and chemokine ligand-receptor axis. These observations suggest an increasing significance of myeloid lineage and related signaling pathways, highlighting its potential as a therapeutic target in ENKTCL.

Targeting surface markers using monoclonal antibodies has been established as one of the most successful therapeutic strategies. Here we have shown that KLRG1 is selectively expressed in mouse and human neoplastic cells and anti-KLRG1 antibody can efficiently eliminate NK-cell tumors in mice. KLRG1, a co-inhibitory receptor belonging to the killer cell lectin-like receptor family, is expressed on a subset of NK and T cells and is postulated to be a marker of differentiation and senescence<sup>25</sup>. Given a monoclonal antibody against KLRG1 (ABC008) is currently under clinical development<sup>26</sup>, KLRG1 targeting and its combination with other immunomodulatory agents are worth further clinical investigation in ENKTCL.

Another important therapeutic target identified in this study is MYC. We have demonstrated that *Myc* is genomically and/or transcriptionally activated in *Trp53*<sup>-/-</sup> tumors and further deregulated in *Trp53*<sup>-/-</sup>*LMP1*<sup>+</sup> tumors. Moreover, MYC inhibition with an eIF4A inhibitor strongly enhanced the efficacy of anti-KLRG1 antibody even in *Trp53*<sup>-/-</sup>*LMP1*<sup>+</sup> tumors. As MYC activation is common in human ENKTCL<sup>9,15</sup>, combined targeting of KLRG1 and MYC can be a promising therapeutic strategy against ENKTCL.

In conclusion, using GEMM recapitulating the human disease, we have delineated the cell-of-origin and microenvironmental changes and exploited potential therapeutic targets, including CXCL16, KLRG1, and MYC, for ENKTCL. These observations prove that our mouse models will serve as valuable tools for elucidating the pathogenic mechanisms and refining diagnostic and therapeutic strategies in ENKTCL.

## Methods

### Mice

B6.129P2-Trp53tm1Brn/J (*Trp53*<sup>fllox/fllox</sup>, catalog number: 008462) and B6.Cg-Ncr1tm1.1(cre)Viv/Or (*Ncr1*-iCre, catalog number: EM05625) were purchased from The Jackson Laboratory and The Institut national de la santé et de la recherche médicale, respectively. *LMP1*<sup>stop</sup> conditional knock-in mice were kindly provided by Dr. Yasui. To generate *Trp53*<sup>-/-</sup> mice, *Trp53*<sup>fllox/fllox</sup> mice were crossed with *Ncr1*-iCre mice. To generate *Trp53*<sup>-/-</sup>*LMP1*<sup>+</sup> mice, *Trp53*<sup>-/-</sup> mice were crossed with *LMP1*<sup>stop</sup> conditional knock-in mice. C57BL/6-SR-PSOX (Cxcl16 knockout) mice (nbio 196) at 8 weeks old were obtained from the Laboratory Animal Resource Bank of the National Institute of Biomedical Innovation, Health, and Nutrition. Female C57BL/6 mice at 8 weeks old were obtained from CLEA Japan, Tokyo, Japan. C57BL/6-SR-PSOX mice were used at 8 weeks old for transplantation experiments, while C57BL/6 mice were used at 8 and 60 weeks old. For *Trp53*<sup>fllox/fllox</sup>, *Trp53*<sup>-/-</sup>, *LMP1*<sup>+</sup>, and *Trp53*<sup>-/-</sup>*LMP1*<sup>+</sup> mice, we used naturally bred cohorts for long-term observation. Additionally, 8-week-old mice from these strains were used for pre-tumor analyses.

All mice were maintained under specific pathogen-free conditions and maintained on a 12-h light/dark cycle at room temperature (22 ± 0.5 °C) with constant humidity (55 ± 10%). Mice were monitored daily and euthanized when they appeared moribund or lost >25% of their body weight. All mouse experiments were approved by the Animals Committee for Animal Experimentation of the National Cancer Center (approval ID: T17-081) and met the Guidelines for Proper Conduct of Animal Experiments (the Science Council of Japan).

### Patient samples

ENKTCL was diagnosed according to the 2008 or 2017 World Health Organization classification depending on the date of diagnosis and biopsies were reviewed by an expert panel of hematopathologists

including those of the French national Lymphopath program<sup>1,27</sup>. All samples were collected from patients with informed consent without compensation, except for already-collected, anonymized samples whose use was permitted by the institutional review board. This study was approved by the National Cancer Center Institutional Review Board and the Ethical Committee of Kurume University and performed in accordance with the Declaration of Helsinki. Sex- and gender-based analyses were not performed.

### Sample preparation

SP and BM cells from the femur and tibia were filtered through a 70  $\mu$ m mesh filter to obtain single-cell suspensions. The samples were then resuspended in PBS containing 3% fetal bovine serum (FBS; Biosera). The suspension was layered over Histopaque (Sigma-Aldrich) and centrifuged at 400  $\times$  g for 20 min. The interphase was subsequently washed with 3% FBS-containing PBS. SG and other site tumor samples were processed using the Tumor Dissociation Kit (Miltenyi Biotec) and the GentleMACS dissociator (Miltenyi Biotec), following the manufacturer's instructions. After centrifugation at 300  $\times$  g for 5 min at 4 °C, the samples were resuspended in red cell lysis buffer (156 mM NH<sub>4</sub>Cl, 20 mM NaHCO<sub>3</sub>, and 0.1 mM EDTA [Nacalai Tesque]) and incubated for 5 min at room temperature. The samples were then centrifuged again, with the supernatant being discarded. PB was treated with 700  $\mu$ L of red cell lysis buffer for 5 min at room temperature. After centrifugation at 300  $\times$  g for 5 min at room temperature, the supernatant was removed. Lysis and washing were repeated twice.

### Analysis of *Trp53*<sup>-/-</sup> and *Trp53*<sup>-/-</sup>*LMP1*<sup>+</sup> mice

CBC was measured using an automated analyzer PCE-210N (ERMA). The SG, SP, and other site tumors were harvested and subjected to further analyses, such as histologic examination, flow cytometric analysis, RNA-seq, and WES. Genomic DNA and RNA were extracted from each organ of the sacrificed mice using the QIAmp DNA Blood Mini Kit and QIAmp RNA Mini Kit (both Qiagen), respectively. Total RNA was reverse transcribed using ReverTra Ace qPCR RT Master Mix (TOYOBO). WT, *Trp53*<sup>-/-</sup>, and *Trp53*<sup>-/-</sup>*LMP1*<sup>+</sup> mice were genotyped using a PCR-based assay. Genomic DNA was isolated from tail biopsies or various subsets of NK cells and subjected to PCR. PCR products were resolved by agarose gel electrophoresis. All steps were followed according to the manufacturer's instructions. PCR protocol is described in Supplementary Data 16 and primers are listed in Supplementary Data 17. The diagnosis of NK-cell tumors was based on CBC, macroscopic and histological examination, immunophenotyping with flow cytometry, evaluation of lymphomagenic potential in secondary transplantation, and whole-exome sequencing.

### Histology

Mouse tissues were fixed overnight in formalin, embedded in paraffin blocks, and sectioned. Tissue sections were stained with hematoxylin and eosin, following standard procedures. Immunohistochemical analysis was performed using 3- $\mu$ m-thick formalin-fixed paraffin-embedded tissue sections from the tissue microarray. Slides were deparaffinized with xylene, followed by ethanol. After rehydration with water, antigen retrieval was performed with Tris-EDTA buffer (pH 9.0) in a microwave oven at 95 °C for 20 min for KLRG1 and CD11c and for 40 min for CD49a, CXCR6, and CXCR3. After cooling and rinsing with buffer, slides were immunostained using the Dako EnVision FLEX detection system (Agilent Technologies) on a Dako Autostainer Link48 (Agilent Technologies). Slides were incubated with antibodies as indicated in Supplementary Data 18. EBV-encoded small RNA (EBER) in situ hybridization was performed using fluorescein isothiocyanate (FITC)-labeled EBV PNA Probe (Agilent Technologies) and anti-FITC antibody (Thermo Fisher Scientific). Human diffuse large B-cell lymphoma samples were used to confirm the specificity of the antibodies (Supplementary Fig. 8). To quantify myeloid cell infiltration, we

counted polymorphonuclear cells in five 60× high-power field for each of two samples of *Trp53*<sup>-/-</sup> and *Trp53*<sup>-/-</sup>*LMPI*<sup>+</sup> tumors.

### Flow cytometry

Antibodies are listed in Supplementary Data 18. Cells were stained with antibodies and 4',6-diamidino-2-phenylindole (DOJINDO) or Zombie Aqua (BioLegend), and were analyzed on LSRFortessa X-20 (BD Biosciences). Various subsets of NK cells were sorted on FACSria II or III Cell Sorter (BD Biosciences). For intracellular flow cytometry of IFN- $\gamma$ , Eomes, and T-bet expressions, we used the eBioscience™ Foxp3/Transcription Factor Staining Buffer Set according to the manufacturer's instructions. Isotype controls were used for intracellular flow cytometry, while fluorescence minus one (FMO) controls were used for all other flow cytometric analyses. Cell cycle and apoptotic status were analyzed using the Fixation/Permeabilization Solution Kit (BD Biosciences), and Annexin V Apoptosis Detection Kit (Thermo Fisher Scientific), respectively, following the manufacturer's instructions. Data were analyzed with FlowJo software (BD Biosciences). The gating strategy is shown in Supplementary Fig. 9.

### In vitro chemokine treatment

To assess the effect of CXCL16 or CXCL9 on the proliferation of tumor cells,  $1 \times 10^5$  Lin<sup>-</sup> *Trp53*<sup>-/-</sup> or Lin<sup>-</sup> *Trp53*<sup>-/-</sup>*LMPI*<sup>+</sup> tumor cells were cultured in RPMI 1640 medium with 50% FBS, 1% PS, and 10 ng/mL IL-15 (PEPROTECH). The cells were treated with either no chemokine (control), 10 ng/mL CXCL16 (R&D Systems), or 100 ng/mL CXCL9 (R&D Systems). After 48 h of culture, the total cell count was determined using the automated cell counter model R1 (OLYMPUS) and normalized relative to the average of the control samples.

### In vitro co-culture with cDC

To assess the effect of cDC on proliferation of *Trp53*<sup>-/-</sup>*LMPI*<sup>+</sup> tumor cells,  $1 \times 10^5$  Lin<sup>-</sup> *Trp53*<sup>-/-</sup>*LMPI*<sup>+</sup> tumor cells were co-cultured with or without  $1 \times 10^4$  WT SP-derived CD11c<sup>+</sup> cDC in RPMI 1640 medium with 50% FBS, 1% PS, and 10 ng/mL IL-15. After 1 week of co- or monoculture, cells were collected and analyzed for KLRG1 and mEGFP (a surrogate marker of LMP1) expressions. The tumor cell counts were determined by multiplying the KLRG1 and GFP positivity by the total cell count measured by the automated cell counter Cell Counter model R1 (OLYMPUS).

### Tumor models and in vivo treatment

Secondary transplantation to confirm the lymphomagenic potential was performed by transferring bulk  $1 \times 10^6$  SP,  $2 \times 10^4$  Lin<sup>-</sup>KLRG1<sup>+</sup>, or  $2 \times 10^4$  Lin<sup>-</sup>KLRG1<sup>-</sup> cells intravenously into lethally irradiated (8.5 Gy) C57BL/6 mice. For in vivo treatment, sub-lethally irradiated (5.5 Gy) mice were transplanted with Lin<sup>+</sup>-depleted  $5 \times 10^5$  tumor cells from secondary tumor of *Trp53*<sup>-/-</sup> #008 (Fig. 6f), primary tumor of *Trp53*<sup>-/-</sup>*LMPI*<sup>+</sup> #025 (Figs. 5l and 6g), and secondary tumor of *Trp53*<sup>-/-</sup>*LMPI*<sup>+</sup> #029 (Figs. 5m and 6i) intravenously. Five mg/kg of anti-CXCL16 antibody (R&D Systems) or their isotype Rat IgG2A antibody (R&D Systems) was administered intraperitoneally every one week beginning from day 5 post-transplantation. Five mg/kg of anti-KLRG1 antibody (BioXcell) or their isotype Syrian hamster IgG antibody (BioXcell) was administered intraperitoneally every three days beginning from day 7 to day 37 post-transplantation. Silvestrol (MCH MedChemexpress) was dissolved in 5% dimethyl sulfoxide and stocked. Each stock was suspended in 5.2% PEG400, 5.2% Tween 80, and 84.6% ddH<sub>2</sub>O, and 0.25 mg/kg of silvestrol was administered intraperitoneally every other day beginning from day 7 to day 37 post-transplantation.

### WES

WES libraries were constructed for 13 (11 primary and 2 secondary) *Trp53*<sup>-/-</sup> and 14 *Trp53*<sup>-/-</sup>*LMPI*<sup>+</sup> tumor samples as well as matched tail

samples (as germline controls) using SureSelectXT Mouse All Exon v1 (Agilent Technologies). The libraries were sequenced on the HiSeq platform (Illumina) with a 150-bp paired-end read protocol at Macrogen.

Sequence alignment and mutation calling were performed using the Genomon pipeline version 2.6.3 (<https://github.com/Genomon-Project/>), as previously described<sup>28,29</sup>. Reads were mapped to the mouse reference genome (GRCm38/mm10). Candidate mutations with (i) Fisher's exact P value <  $10^{-15}$ ; (ii) EBCall<sup>30</sup> P value <  $10^{-3}$ ; (iii)  $\geq 4$  variant reads in tumor samples; (iv) mutant allele frequency  $\geq 0.05$  in tumor samples; and (v) allele frequency in germline control < 0.05 were adopted and further filtered by excluding (i) synonymous single nucleotide variants; (ii) variants only present in unidirectional reads; (iii) variants occurring in repetitive genomic regions; (iv) variants in mouse single nucleotide polymorphism database (NCBI dbSNP137, 138, and 140); or (v) variants detected in multiple tumor samples, which were considered to be germline. Finally, mutations were manually checked by Integrative Genomics Viewer (IGV)<sup>31</sup> version 2.11.4. In the subsequent analysis, tumor samples with >3 mutations were considered as clonally confirmed. Pearson's correlation analysis was performed to investigate the association between the median mutant allele frequency and the proportion of Lin<sup>-</sup>CD122<sup>+</sup>KLRG1<sup>+</sup> cells by flow cytometry in tumor samples. The median mutant allele frequency for samples in which no mutations were detected was set to zero.

CNAs were detected using CNVkit<sup>32</sup> version 0.9.9, using the above-mentioned tail samples from 9 *Trp53*<sup>-/-</sup> and 10 *Trp53*<sup>-/-</sup>*LMPI*<sup>+</sup> male mice as a panel of normal samples. After estimating tumor purity (at  $\geq 0.3$ ) from mutant allele frequencies, absolute integer copy numbers were determined for each sample using 'call' command. CNAs were filtered to exclude (i) chromosome X deletions in males; and (ii) CNAs with  $\leq 10$  Mb in length, unless they were homozygous deletions (copy number = 0) or high amplifications (copy number > 5). Finally, all detected CNAs were curated by visual inspection.

### Mutational signature

SigProfilerMatrixGenerator version 1.1.23 was used to categorize mutations into 96 classes and plot the mutational pattern, with the parameter "exome = True". We decomposed the overall mutational pattern into 72 signatures from the COSMIC v3.1 compendium using SigProfilerExtractor version 1.1.0 with the default setting, and the proportion of clock-like (SBS1 and SBS5) and reactive oxygen species (SBS17a, SBS17b, and SBS18) signatures were calculated.

To compare the mutation pattern between mouse NK-cell tumors and human ENKTCL, we analyzed previously published WES data of 66 ENKTCL cases from our (accession number EGAS00001006906) and other studies (SRP057085 and SRP049695)<sup>33</sup>. Mutation calling and mutational signature analysis were performed in a similar manner to the mouse analysis.

### Bulk RNA-seq and analysis

RNA concentration and RNA integrity number (RIN) were measured by 4200 TapeStation (Agilent Technologies). RNA-seq libraries were prepared for samples with RIN  $\geq 7$  using NEBNext Ultra II RNA Library Prep Kit for Illumina (New England Biolabs) and NEBNext Poly(A) mRNA Magnetic Isolation Module (New England Biolabs) for mouse, according to the manufacturer's instructions. The libraries were sequenced on the HiSeq platform (Illumina) with a 150-bp paired-end read protocol at Macrogen.

In mice, SG, SP, and BM samples from 5 WT and 3 *Trp53*<sup>-/-</sup> mice at the pre-tumor stage (8 weeks old) as well as 4 *Trp53*<sup>-/-</sup> clonally confirmed tumors were analyzed. Mapping and expression analyses were conducted using the Genomon pipeline version 2.6.3 (<https://github.com/Genomon-Project/>) with the mouse reference genome GRCm38/mm10. Expression for RefSeq genes was calculated as raw read counts

using featureCounts<sup>34</sup>. Differentially expressed genes between the two groups were detected using the edgeR<sup>35</sup> version 3.36.0, with the raw read count matrix. To perform dimensionality reduction and clustering, we first calculated transcripts per million (TPM) values from raw read counts and performed principal component analysis (PCA) using  $\log_2(\text{TPM} + 1)$  value. Then, the resultant clusters were visualized on a UMAP (uniform manifold approximation and projection) embedding using the umap version 0.2.10 with the first 10 principal components.

In humans, RNA-seq data for 21 ENKTCL tumors and 3 normal NK cells from healthy donors were described in our previous study (accession number EGAS00001006906)<sup>33</sup>. Publicly available RNA-seq data for 20 ENKTCL tumors and 3 normal tonsils from ENKTCL patients and 1 normal NK cell from a healthy donor (accession number SRP057085<sup>7</sup>, SRP049695<sup>36</sup>, and GSE190924<sup>37</sup>) were also obtained from the National Center for Biotechnology Information Sequence Read Archive. Mapping and expression analyses were conducted using the Genomon pipeline version 2.6.2 with the human reference genome hs37d5, which included the EBV genomic sequence (NC\_007605). Expression for RefSeq genes and *LMPI* were calculated as fragments per kilobase of exon per million reads mapped values (FPKM). The batch effect among datasets was corrected using the ComBat function in the R package sva (version 3.42.0) while preserving cell type-specific effects<sup>38</sup>. Adjusted expression values below zero were subsequently set to zero. A detailed analysis of the human RNA-seq dataset was published elsewhere<sup>33</sup>.

### Functional enrichment analysis in bulk RNA-seq

GSEA version 4.1.0 was conducted using hallmark, Reactome, and WikiPathways gene sets from the mouse and human Molecular Signatures Database (MSigDB) (version 2022.1) for mice and humans, respectively<sup>39</sup>. Raw read counts normalized by the trimmed mean of the M-values method using edgeR (for mouse) and FPKM values (for human) were used as input. Phenotype permutation was used when at least seven samples were available for each phenotype, otherwise gene set permutation was chosen. Gene sets with a false discovery rate (FDR) < 0.25 and < 0.05 were considered significantly enriched for phenotype permutation and gene set permutation, respectively. Tissue-resident and circulating NK-cell signatures were created based on the previous study comparing CD56<sup>bright</sup>CD16<sup>-</sup> and CD56<sup>dim</sup>CD16<sup>+</sup> NK-cell subsets in humans<sup>40</sup>.

### Immune cell deconvolution using CIBERSORTx

To estimate the proportions of different immune cell types, the FPKM values were uploaded to the CIBERSORTx online platform (<https://cibersortx.stanford.edu/>) for each cell type. The LM22 signature matrix was used with the following parameters; quantile normalization disabled, absolute run mode, and 100 permutations. As discriminating tumor cells and normal T and NK cells is difficult, the proportion in nonmalignant cells was estimated after excluding T and NK cells.

### Library preparation and sequencing for scRNA-seq analysis

Frozen mouse tumor samples were rapidly thawed, followed by staining with TruStain FcX PLUS (anti-mouse CD16/32) Antibody (BioLegend) according to the manufacturer's instructions. Subsequently, cells were stained with anti-CD45 antibody (BioLegend) and hash-tag antibody (Total-seqB, BioLegend). In each sample, 15,000 CD45<sup>+</sup> cells were sorted and multiplexed at two samples. scRNA-seq libraries were prepared using the Chromium Next GEM Single Cell 3' Kit v3.1 (PN-1000268), Chromium Next GEM Chip G Single Cell Kit (PN-1000120), Dual Index Kit TT Set A (PN-1000215), according to manufacturer's instructions (CG000315 Rev E) (10x Genomics). These libraries were sequenced on the NovaSeq 6000 platform (Illumina) to yield paired-end 150 bp reads at Macrogen.

### Preprocessing of single-cell data

As previously described<sup>41</sup>, raw scRNA-seq results were demultiplexed and converted to FASTQ format using 10x Genomics Cell Ranger (version 5.0.1). scRNA-seq data were aligned to the reference genome created using 'cellranger mkref' with mouse reference (GRCm38) and *LMPI* (NC\_007605). Unique molecular identifiers (UMI) of scRNA-seq data were counted using 'cellranger count' and aggregated using 'cellranger aggr'. Gene-barcode matrix was then analyzed using Seurat (version 4.3.0)<sup>42</sup>. To exclude low-quality cells, we removed (i) cells with  $\leq 200$  or  $\geq 8000$  detected genes, and (ii) cells with  $\geq 10\%$  of transcripts from mitochondrial genes.

The UMI count matrix of scRNA-seq data was normalized, scaled, and centered using 'SCTransform' function. Then, 3000 most variable genes were selected based on standardized variance, from which TCR (*Trav*, *Trbv*, *Trdv*, and *Trgv*), immunoglobulin (*Igkc*, *Igkv*, *Igcl*, *Iglv*, *Ighg*, *Ighv*, *Igha*, *Ighm*, and *Jchain*), ribosomal (*Rps* and *Rpl*), and mitochondrial variable genes were excluded. Dimensionality reduction was performed based on PCA using the 'RunPCA' function. Then, a K-nearest neighbor (KNN) graph was constructed based on the result of PCA using the 'FindNeighbors' function. To group the cells into different clusters, a smart local moving clustering algorithm was applied based on the KNN graph using the 'FindClusters' function with a resolution of 0.2. Then, we removed doublets detected by DoubletFinder package (version 2.0.3)<sup>43</sup>. The remaining 84,550 cells were subsequently analyzed.

### Identification of cell clusters on scRNA-seq

For the remaining cells, the KNN graph-based clustering was repeated with a resolution of 0.11. For visualization, the dimensionality was further reduced using UMAP<sup>44</sup> with the 'RunUMAP' function. Seven malignant and 13 nonmalignant cell clusters were identified. Malignant cell clusters were classified into *LMPI* negative or positive. Nonmalignant cell clusters were assigned to known broad cell types (T/NK, B, and myeloid cells) based on the expression of canonical lineage markers, while the remaining cells were classified into others.

We applied the same normalization, dimensionality reduction, and clustering pipeline as described above to each dataset of T/NK, B, and myeloid cells to identify subclusters within these broad cell types. T/NK-cell cluster was subclassified into CD4<sup>+</sup> T, CD8<sup>+</sup> T, and NK cells. Then, both CD4<sup>+</sup> T and CD8<sup>+</sup> T cells were processed again using the same pipeline and further classified into more specific subclusters. These individual subclusters were assigned to known subsets based on the expression of representative mRNA markers.

To quantify the enrichment of cell clusters across organs (SG/Other and SP) and groups (pre-tumor, *Trp53*<sup>-/-</sup> tumor, and *Trp53*<sup>-/-</sup> *LMPI*<sup>+</sup> tumor), we compared the observed and expected cell numbers in each cluster by computing the  $R_{o/e}$  value using the epitools package (version 0.5-10.1) according to the following formula:  $R_{o/e} = \text{Observed/Expected}$ , where the expected cell numbers for each combination of cell clusters and organs were obtained from the chi-square test. Statistical significance was assessed using the binomial test for each cell cluster.

### Functional enrichment analysis for differentially expressed mRNAs in scRNA-seq

To identify significantly enriched pathways, GSEA was performed using ClusterProfiler package (version 4.6.2) and hallmark, Reactome, and WikiPathways gene sets from the mouse MSigDB (version 2022.1). Gene lists were generated by the Wilcoxon rank sum test between two clusters/subclusters using the Seurat 'FindMarkers' function, and genes in each list were ranked according to  $\log_2(\text{fold change})$  in descending order. Statistical significance was calculated by a phenotype permutation test and FDR < 0.1 was considered significant.

## Inference of cell-cell communication and signaling pathways

Cell-cell communication analysis was performed using the R package CellChat (version 1.6.1)<sup>45</sup>. Normalized mRNA expression data derived from *Trp53*<sup>-/-</sup> and *Trp53*<sup>-/-</sup>*LMP1*<sup>+</sup> tumors were used to create the CellChat object. We applied the recommended preprocessing functions with default parameters. Cell-cell communication and signaling networks of individual ligand-receptor pairs were inferred using the CellChatDB-mouse database and depicted as chord diagrams using the 'netVisual\_individual' function. Outgoing or incoming signals across cell clusters were calculated and visualized using the 'netAnalysis\_signalingRole\_heatmap' function. Information flow for each signaling, which is defined by the sum of communication probability among all pairs of cell clusters in the inferred network, was compared between *Trp53*<sup>-/-</sup> and *Trp53*<sup>-/-</sup>*LMP1*<sup>+</sup> tumors and visualized using the 'rankNet' function.

## Reagents

All commercial reagents used in this study are listed in Supplementary Data 19.

## Statistical analysis

Statistical analyses were performed with R3.6.1 software (The R Foundation for Statistical Computing). Comparison of continuous data was performed using the two-sided Welch's t-test unless otherwise specified. Survival analyses were conducted using the log-rank test. All measurements shown are distinct biological replicates unless otherwise noted.

## Reporting summary

Further information on research design is available in the Nature Portfolio Reporting Summary linked to this article.

## Data availability

Mouse RNA-seq, WES, and scRNA-seq data have been deposited in the DNA Data Bank of Japan (DDBJ) BioProject database under accession number [PRJDB16976](https://www.ncbi.nlm.nih.gov/bioproject/PRJDB16976). The human data from other studies used in this paper are available in the European Genome-phenome Archive under accession number [EGAS00001006906](https://www.ebi.ac.uk/ena/browser/view/EGAS00001006906), the NCBI Sequence Read Archive under accession numbers [SRP057085](https://www.ncbi.nlm.nih.gov/sra/SRR057085) and [SRP049695](https://www.ncbi.nlm.nih.gov/sra/SRR049695), and the NCBI Gene Expression Omnibus under accession number [GSE190924](https://www.ncbi.nlm.nih.gov/geo/query/acc.cgi?acc=GSE190924) (<https://www.ncbi.nlm.nih.gov/geo/query/acc.cgi?acc=GSE190924>). The remaining data are available within Supplementary Information and Source Data file. Source data are provided with this paper.

## Code availability

The original code used for single-cell analyses has been deposited in Github: <https://github.com/nccmo/mouse-NK-lymphoma-2024> and in Zenodo: <https://doi.org/10.5281/zenodo.13837293>. All other codes used in this study are available upon request from the corresponding author.

## References

- S. H. Swerdlow, et al. *WHO Classification of Tumours of Haematopoietic and Lymphoid Tissues* (International Agency for research on cancer, 2017).
- Tse, E., Zhao, W.-L., Xiong, J. & Kwong, Y.-L. How we treat NK/T-cell lymphomas. *J. Hematol. Oncol.* **15**, 74 (2022).
- Yamaguchi, M., Suzuki, R. & Oguchi, M. Advances in the treatment of extranodal NK/T-cell lymphoma, nasal type. *Blood* **131**, 2528–2540 (2018).
- Münz, C. Latency and lytic replication in Epstein-Barr virus-associated oncogenesis. *Nat. Rev. Microbiol.* **17**, 691–700 (2019).
- de Mel, S., Hue, S. S., Jeyasekharan, A. D., Chng, W. J. & Ng, S. B. Molecular pathogenic pathways in extranodal NK/T cell lymphoma. *J. Hematol. Oncol.* **12**, 33 (2019).
- Blossom, D., Shannon, C. K. & Nancy, R.-T. Epstein-Barr virus: biology and clinical disease. *Cell* **185**, 3652–3670 (2022).
- Jiang, L. et al. Exome sequencing identifies somatic mutations of DDX3X in natural killer/T-cell lymphoma. *Nat. Genet.* **47**, 1061–1066 (2015).
- Kataoka, K. et al. Frequent structural variations involving programmed death ligands in Epstein-Barr virus-associated lymphomas. *Leukemia* **33**, 1687–1699 (2019).
- Xiong, J. et al. Genomic and transcriptomic characterization of natural killer T cell lymphoma. *Cancer Cell* **37**, 403–419.e406 (2020).
- Cho, J. et al. Immune subtyping of extranodal NK/T-cell lymphoma: a new biomarker and an immune shift during disease progression. *Mod. Pathol.* **33**, 603–615 (2020).
- Kim, S. J. et al. Avelumab for the treatment of relapsed or refractory extranodal NK/T-cell lymphoma: an open-label phase 2 study. *Blood* **136**, 2754–2763 (2020).
- Nagata, H. et al. Characterization of novel natural killer (NK)-cell and gammadelta T-cell lines established from primary lesions of nasal T/NK-cell lymphomas associated with the Epstein-Barr virus. *Blood* **97**, 708–713 (2001).
- Mundy-Bosse, B. L. et al. Identification and targeting of the developmental blockade in extranodal natural killer/T-cell lymphoma. *Blood Cancer Discov.* **3**, 154–169 (2022).
- Peng, H. & Tian, Z. Diversity of tissue-resident NK cells. *Semin Immunol.* **31**, 3–10 (2017).
- Oishi, N. et al. Genetic and immunohistochemical profiling of NK/T-cell lymphomas reveals prognostically relevant BCOR-MYC association. *Blood Adv.* **7**, 178–189 (2023).
- Vaysberg, M., Lambert, S. L., Krams, S. M. & Martinez, O. M. Activation of the JAK/STAT pathway in Epstein Barr virus-associated posttransplant lymphoproliferative disease: role of interferon-gamma. *Am. J. Transpl.* **9**, 2292–2302 (2009).
- Cerezo, M. et al. Translational control of tumor immune escape via the eIF4F-STAT1-PD-L1 axis in melanoma. *Nat. Med.* **24**, 1877–1886 (2018).
- Gordon, S. M. et al. The transcription factors T-bet and Eomes control key checkpoints of natural killer cell maturation. *Immunity* **36**, 55–67 (2012).
- Kaye, K. M., Izumi, K. M. & Kieff, E. Epstein-Barr virus latent membrane protein 1 is essential for B-lymphocyte growth transformation. *Proc. Natl Acad. Sci. USA* **90**, 9150–9154 (1993).
- Zhang, B. et al. Immune surveillance and therapy of lymphomas driven by Epstein-Barr virus protein LMP1 in a mouse model. *Cell* **148**, 739–751 (2012).
- van Vlerken-Ysla, L., Tyurina, Y. Y., Kagan, V. E. & Gabilovich, D. I. Functional states of myeloid cells in cancer. *Cancer Cell* **41**, 490–504 (2023).
- Wang, H. et al. High numbers of CD68+ tumor-associated macrophages correlate with poor prognosis in extranodal NK/T-cell lymphoma, nasal type. *Ann. Hematol.* **94**, 1535–1544 (2015).
- Walzer, T., Dalod, M., Robbins, S. H., Zitvogel, L. & Vivier, E. Natural killer cells and dendritic cells: 'l'union fait la force. *Blood* **106**, 2252–2258 (2005).
- Degli-Esposti, M. A. & Smyth, M. J. Close encounters of different kinds: dendritic cells and NK cells take centre stage. *Nat. Rev. Immunol.* **5**, 112–124 (2005).
- Henson, S. M. & Akbar, A. N. KLRG1—more than a marker for T cell senescence. *Age* **31**, 285–291 (2009).
- Naddaf, E. Inclusion body myositis: update on the diagnostic and therapeutic landscape. *Front. Neurol.* **13**, 1020113 (2022).
- Sabattini, E., Bacci, F., Sagromoso, C. & Pileri, S. A. WHO classification of tumours of haematopoietic and lymphoid tissues in 2008: an overview. *Pathologica* **102**, 83–87 (2010).

28. Tabata, M. et al. Inter- and intra-tumor heterogeneity of genetic and immune profiles in inherited renal cell carcinoma. *Cell Rep.* **42**, 112736 (2023).
29. Kataoka, K. et al. Integrated molecular analysis of adult T cell leukemia/lymphoma. *Nat. Genet.* **47**, 1304–1315 (2015).
30. Shiraishi, Y. et al. An empirical Bayesian framework for somatic mutation detection from cancer genome sequencing data. *Nucleic Acids Res.* **41**, e89 (2013).
31. Robinson, J. T. et al. Integrative genomics viewer. *Nat. Biotechnol.* **29**, 24–26 (2011).
32. Talevich, E., Shain, A. H., Botton, T. & Bastian, B. C. CNVkit: genome-wide copy number detection and visualization from targeted DNA sequencing. *PLoS Comput. Biol.* **12**, e1004873 (2016).
33. Ito, Y. et al. Comprehensive genetic profiling reveals frequent alterations of driver genes on the X chromosome in extranodal NK/T-cell lymphoma. *Cancer Res.* **84**, 2181–2201 (2024).
34. Liao, Y., Smyth, G. K. & Shi, W. featureCounts: an efficient general purpose program for assigning sequence reads to genomic features. *Bioinformatics* **30**, 923–930 (2014).
35. Robinson, M. D., McCarthy, D. J. & Smyth, G. K. edgeR: a Bioconductor package for differential expression analysis of digital gene expression data. *Bioinformatics* **26**, 139–140 (2010).
36. Küçük, C. et al. Activating mutations of STAT5B and STAT3 in lymphomas derived from  $\gamma\delta$ -T or NK cells. *Nat. Commun.* **6**, 6025 (2015).
37. Zhou, J. et al. Super-enhancer-driven TOX2 mediates oncogenesis in natural killer/T cell lymphoma. *Mol. Cancer* **22**, 69 (2023).
38. Johnson, W. E., Li, C. & Rabinovic, A. Adjusting batch effects in microarray expression data using empirical Bayes methods. *Bio-statistics* **8**, 118–127 (2007).
39. Subramanian, A. et al. Gene set enrichment analysis: a knowledge-based approach for interpreting genome-wide expression profiles. *Proc. Natl Acad. Sci. USA* **102**, 15545–15550 (2005).
40. Dogra, P. et al. Tissue determinants of human NK cell development, function, and residence. *Cell* **180**, 749–763 e713 (2020).
41. Koya, J. et al. Single-cell analysis of the multicellular ecosystem in viral carcinogenesis by HTLV-1. *Blood Cancer Discov.* **2**, 450–467 (2021).
42. Butler, A., Hoffman, P., Smibert, P., Papalexi, E. & Satija, R. Integrating single-cell transcriptomic data across different conditions, technologies, and species. *Nat. Biotechnol.* **36**, 411–420 (2018).
43. McGinnis, C. S., Murrow, L. M. & Gartner, Z. J. DoubletFinder: doublet detection in single-cell RNA sequencing data using artificial nearest neighbors. *Cell Syst.* **8**, 329–337.e4 (2019).
44. Becht, E. et al. Dimensionality reduction for visualizing single-cell data using UMAP. *Nat. Biotechnol.* <https://doi.org/10.1038/nbt.4314> (2018).
45. Jin, S. et al. Inference and analysis of cell-cell communication using CellChat. *Nat. Commun.* **12**, 1088 (2021).

## Acknowledgements

This work was supported by Japan Society for the Promotion of Science (JSPS) KAKENHI (JP21H05051 [K.K.] and JP22H03108 [J.K.]), Japan Science and Technology Agency Moonshot R&D Program (JPMJMS2022 [K.K.]), Japan Agency for Medical Research and Development (JP20ck0106442 [J.K.] and JP23gm1810002 [K.K.]), SGH Foundation [J.K.], Princess Takamatsu Cancer Research Fund [K.K.], MSD Life

Science Foundation [K.K.], and Takeda Science Foundation [K.K.], Nippon Shinyaku Co., Ltd. Research Grant [J.K.]. We thank Fumie Ueki, Yoko Hokama, and Yoshiko Ito for their technical assistance. The sequencing resources were partly provided by Fundamental Innovative Oncology Core at the National Cancer Center. The supercomputing resources were provided by the Human Genome Center, the Institute of Medical Science, The University of Tokyo.

## Author contributions

J.K. and T.T. performed functional assays. K.Y., S.S., and K. Murakami supported functional assays. K. Mizuno, H.K., Y.I., M.Y., and L.C. performed sequencing data analyses. Y.K., Y. Saito, M.T., K.C., A.O., and Y. Shiraishi assisted sequencing data analyses. T.Y. created *LMPI\** mice. K.N., H.M. and K.O. performed a pathological assessment. A.M., R.L., S.C., A.J., O.H., L.L., O.T., G.D., P.G., and L.C. prepared samples. J.K., T.T., and K.K. generated figures and tables and wrote the manuscript. K.K. led the entire project. All authors participated in discussions and interpretation of the data and results.

## Competing interests

The authors declare no competing interests.

## Additional information

**Supplementary information** The online version contains supplementary material available at <https://doi.org/10.1038/s41467-024-53376-1>.

**Correspondence** and requests for materials should be addressed to Keisuke Kataoka.





**Peer review information** *Nature Communications* thanks Nicholas Huntington and the other, anonymous, reviewer(s) for their contribution to the peer review of this work. A peer review file is available.

**Reprints and permissions information** is available at <http://www.nature.com/reprints>

**Publisher's note** Springer Nature remains neutral with regard to jurisdictional claims in published maps and institutional affiliations.

**Open Access** This article is licensed under a Creative Commons Attribution-NonCommercial-NoDerivatives 4.0 International License, which permits any non-commercial use, sharing, distribution and reproduction in any medium or format, as long as you give appropriate credit to the original author(s) and the source, provide a link to the Creative Commons licence, and indicate if you modified the licensed material. You do not have permission under this licence to share adapted material derived from this article or parts of it. The images or other third party material in this article are included in the article's Creative Commons licence, unless indicated otherwise in a credit line to the material. If material is not included in the article's Creative Commons licence and your intended use is not permitted by statutory regulation or exceeds the permitted use, you will need to obtain permission directly from the copyright holder. To view a copy of this licence, visit <http://creativecommons.org/licenses/by-nc-nd/4.0/>.

© The Author(s) 2024

Junji Koya <sup>1,2,20</sup>, Tomohiko Tanigawa<sup>1,2,20</sup>, Kota Mizuno <sup>1,2</sup>, Haryoon Kim<sup>1,2</sup>, Yuta Ito <sup>1,3</sup>, Mitsuhiro Yuasa<sup>1,4</sup>, Kentaro Yamaguchi<sup>1,2</sup>, Yasunori Kogure<sup>1</sup>, Yuki Saito <sup>1,5</sup>, Sumito Shingaki<sup>1</sup>, Mariko Tabata<sup>1,6</sup>, Koichi Murakami<sup>1,2</sup>, Kenichi Chiba<sup>7</sup>, Ai Okada<sup>7</sup>, Yuichi Shiraishi <sup>7</sup>, Amira Marouf<sup>8</sup>, Raphaël Liévin<sup>8</sup>, Sammara Chaubard<sup>9</sup>, Arnaud Jaccard<sup>9</sup>,

**Olivier Hermine<sup>8,10</sup>, Laurence de Leval<sup>11</sup>, Olivier Tournilhac<sup>12</sup>, Gandhi Damaj<sup>13</sup>, Philippe Gaulard<sup>14,15</sup>, Lucile Couronné<sup>8,16</sup>, Teruhito Yasui<sup>17,18</sup>, Kazutaka Nakashima<sup>19</sup>, Hiroaki Miyoshi<sup>19</sup>, Koichi Ohshima<sup>19</sup> & Keisuke Kataoka<sup>1,2</sup>** ✉

<sup>1</sup>Division of Molecular Oncology, National Cancer Center Research Institute, Tokyo, Japan. <sup>2</sup>Division of Hematology, Department of Medicine, Keio University School of Medicine, Tokyo, Japan. <sup>3</sup>Division of Clinical Oncology and Hematology, Department of Internal Medicine, The Jikei University School of Medicine, Tokyo, Japan. <sup>4</sup>Department of Pathology, Graduate School of Medicine, The University of Tokyo, Tokyo, Japan. <sup>5</sup>Department of Gastroenterology, Keio University School of Medicine, Tokyo, Japan. <sup>6</sup>Department of Urology, Graduate School of Medicine, The University of Tokyo, Tokyo, Japan. <sup>7</sup>Division of Genome Analysis Platform Development, National Cancer Center Research Institute, Tokyo, Japan. <sup>8</sup>Laboratory of cellular and molecular mechanisms of hematological disorders and therapeutic implications, INSERM UMR\_S 1163, Imagine Institute, Université Paris Cité, Paris, France. <sup>9</sup>Hematology department, Limoges University Hospital, Limoges, France. <sup>10</sup>Hematology Department, Necker Children's Hospital, Assistance Publique - Hôpitaux de Paris (APHP), Paris, France. <sup>11</sup>Institute of Pathology, Department of Laboratory Medicine and Pathology, Lausanne University Hospital and Lausanne University, Lausanne, Switzerland. <sup>12</sup>Department of Hematology, Clermont-Ferrand University Hospital, Clermont Auvergne University, Clermont-Ferrand, France. <sup>13</sup>Department of Hematology, Caen University Hospital, Normandy University, Caen, France. <sup>14</sup>University Paris Est Créteil, INSERMU955, IMRB, Créteil, France. <sup>15</sup>Pathology Department, Henri Mondor University Hospital, Assistance Publique -Hôpitaux de Paris (APHP), Créteil, France. <sup>16</sup>Laboratory of Onco-Hematology, Necker Children's Hospital, Assistance Publique -Hôpitaux de Paris (APHP), Paris, France. <sup>17</sup>Laboratory of Infectious Diseases and Immunity, Microbial Research Center for Health and Medicine, National Institutes of Biomedical Innovation, Health and Nutrition, Ibaraki City, Japan. <sup>18</sup>Division of Molecular Psychoneuroimmunology, Institute for Genetic Medicine, Hokkaido University, Sapporo, Japan. <sup>19</sup>Division of Pathology, Kurume University, Fukuoka, Japan. <sup>20</sup>These authors contributed equally: Junji Koya, Tomohiko Tanigawa. ✉e-mail: [kkataoka-ky@umin.ac.jp](mailto:kkataoka-ky@umin.ac.jp)